



A New Method for Calibration of Gain Variation in a Detector System

Shohei Goda^{ID} and Taro Matsuo

Department of Earth and Space Science, Graduate School of Science, Osaka University, 1-1, Machikaneyamacho, Toyonaka, Osaka 560-0043, Japan

Received 2018 July 4; revised 2018 October 17; accepted 2018 October 22; published 2018 November 30

Abstract

Transit spectroscopy of habitable planets orbiting late-type stars requires high relative spectrophotometric accuracy between wavelengths during transit/eclipse observation. The spectrophotometric signal is affected not only by image movement and deformation due to wavefront error but also by electrical variation in the detector system. These time-variation components, coupled to the transit signal, distort the measurements of atmospheric composition in transit spectroscopy. Here we propose a new concept for improvement of spectrophotometric accuracy through the calibration of the time-variation components in the detector system by developing densified pupil spectroscopy that provides multiple spectra of the star–planet system. Owing to a group of pixels exposed by the object light (i.e., science pixels), pixel-to-pixel variations can be smoothed out through an averaging operation; thus, only common time-variation components over the science pixels remain. In addition, considering that the detector plane is optically conjugated to the pupil plane, a pupil mask can completely block astronomical light coming into residual pixels. The common time-variation components are reconstructed with the residual pixels and reduced into a random term. Applying the densified pupil spectrograph with a mid-infrared detector system to a large space cryogenic telescope such as the *Origins Space Telescope*, we show that the system nearly achieves photon noise-limited performance and detects absorption features through transmission spectroscopy and secondary eclipse of terrestrial planets orbiting M-type stars at 10 pc with 60 transit observations. Thus, the proposed method contributes to the measurement of planetary habitability and biosignatures of the nearby transiting habitable candidates.

Key words: instrumentation: spectrographs – methods: data analysis – planets and satellites: atmospheres – planets and satellites: terrestrial planets – techniques: spectroscopic

1. Introduction

Characterization of Earth-like planets’ atmospheres in the mid-infrared wavelength is an important approach to search for life in the universe. A sign of a nonequilibrium atmosphere that indicates biological activity on a planet can be confirmed through measurements of both oxidized species such as O₂ and O₃ and reduced species such as CH₄ and N₂O (Lovelock 1965; Sagan et al. 1993). Most of these species produce strong absorption lines in the mid-infrared wavelength range: O₃ at 9.6 μm, CH₄ at 3.3 and 7.7 μm, and N₂O at 7.8 μm. Note that the thermodynamic disequilibrium atmosphere with gases of CO and CH₄ can be formed through abiotic processes at room temperature (Kasting et al. 2014); the combination of O₂ (O₃) and CH₄ or O₂ (O₃) and N₂O is a reliable indicator of biological activity (e.g., Kaltenegger 2017). The ozone gas is also a good tracer for the presence of life on a planet whose surface is undergoing an oxidization process because the deep absorption at 9.6 μm is formed even under low oxygen concentration in the atmosphere (Rugheimer & Kaltenegger 2018). Considering the oxidation history of the Earth’s surface by oxygenic photosynthesis (e.g., Kump & Barley 2007; Lyons et al. 2014), we can investigate whether the oxidation history on a planet’s surface corresponds to biological activity similar to that of Earth.

There are two main approaches for atmospheric spectroscopy of habitable terrestrial planets: direct imaging that directly detects the planet’s light embedded in the bright halo of a star (e.g., Cash 2006; Trauger & Traub 2007) and transit spectroscopy that detects additional absorption by atmospheric molecules of a transiting planet while the planet passes in front of the primary star (e.g., Charbonneau et al. 2002; Swain et al. 2008). In

addition, we can detect the emission by making the difference between before/after and during the eclipse (e.g., Deming et al. 2005; Charbonneau et al. 2008). Direct imaging in the mid-infrared wavelength requires a nulling interferometer that comprises two collecting apertures with a baseline of a few hundred m (e.g., Bracewell 1978; Angel & Woolf 1997; Matsuo et al. 2011). This separation improves the inner working angle, as well as the spatial resolution in that wavelength range, by introducing an achromatic phase shift between the two beams so that the stellar light is suppressed. On the other hand, although the transit spectroscopy can be performed only when an observing condition is met, in which an observer, a host star, and its orbiting planet are aligned, we do not essentially need an interferometer for higher spatial resolution because the transit observation is independent of the angular distance between the host star and its planet. The species related to the biomarkers and planetary habitability in the stratosphere of the Earth also produce absorption lines in the mid-infrared range (Kaltenegger & Traub 2009); these gases increasingly tend to be detected from the transmission spectrum (e.g., Perryman 2011; Barstow & Irwin 2016). Furthermore, since the contrast between the cool sunspot or bright facula and the stellar photosphere becomes smaller as the wavelength is longer, the systematic error arising from the stellar activity can be reduced in that range (Ballerini et al. 2012). Thus, the transit spectroscopy in the mid-infrared wavelength opens a new path toward characterization of the Earth-like planets.

Transit observations in the mid-infrared region have been conducted by the *Spitzer Space Telescope* and have revealed the temperature distribution and atmospheric circularization on the surface of the transiting planets (e.g., Knutson et al. 2007; Stevenson et al. 2014; Kataria et al. 2016), as well as the

atmospheric composition of hot Jupiters (e.g., Tinetti et al. 2007; Madhusudhan & Seager 2009). The *James Webb Space Telescope (JWST)*, as the successor to the *Spitzer Space Telescope*, is able to perform transit spectroscopy of sub-Neptunes and super-Earths owing to its large aperture (e.g., Deming et al. 2009; Greene et al. 2016). However, since the spectrophotometric accuracy of *JWST* in the mid-infrared region is expected to be limited by several dozen ppm due to various instrumental systematic effects, even under small telescope pointing jitter (Beichman et al. 2014), it is difficult (but not impossible) to implement spectroscopy of nearby terrestrial planets in the habitable zones around late-type stars such as the Trappist-1 system (Gillon et al. 2017) through coaddition of the multiple transmission spectra (Beichman & Greene 2018). Although several advanced data analyses for the space telescopes, including the *Spitzer Space Telescope*, have been proposed (e.g., Waldmann et al. 2013; Morello et al. 2016), whether such systematic errors can be reduced down to 10 ppm with sophisticated techniques is still unknown. Thus, the instrumental systematic components should be carefully treated and accurately calibrated for transit spectroscopy of the Earth-like planets with future space telescopes.

Image movement and deformation of the point-spread function (PSF) on intra- and interpixel sensitivity variations (Barron et al. 2007; Ingalls et al. 2012) due to the telescope pointing jitter and wavefront errors (WFEs) generates time-variable components that affect the observational data from space (Carey et al. 2014; Zellem et al. 2014). This occurs because the spectrum is formed on the focal plane for general-purpose spectrographs, and the WFEs on the pupil plane directly deform the PSF. Densified pupil spectroscopy has been proposed for minimization of the instrumental systematic noise caused by WFEs through acquiring multiple spectra of the primary mirror on the detector plane (Matsuo et al. 2016). Pupil masks that form apodized PSFs on a field stop have been also proposed to reduce the photometric variation arising from the field-stop loss coupled with the pointing jitter and WFEs (Itoh et al. 2017).

The systematic errors are generated by electric instability in a semiconductor device and a readout integrated circuit (ROIC), as well as the PSF movement and deformation due to the WFEs in the optical system. According to previous studies of the semiconductor devices and ROICs developed for the mid-infrared observations, the systematic component related to the electric instability is mainly divided into three parts. The first photometric variation is observed as a steep ramp of a small percentage at the beginning of the transit observations and a fall of 0.1 percentage point over a timescale of 10–20 hr after the ramp (e.g., Young et al. 2003; Crossfield et al. 2012). We hereafter refer to the long-term fall of the detector gain as “fallback.” Note that this phenomenon does not always occur, but we consider the signal with this effect in the present paper. The ramp is thought to be caused by the variation of the ratio of the number of incident photons to that of photoelectrons that arrive at the ROIC, i.e., the effective gain variation (Knutson et al. 2009; Seager & Deming 2009; Agol et al. 2010). The effective gain variation arises from the change of the number of photoelectrons trapped due to detector impurities; as the photoelectrons bury the holes produced by the detector impurities, they increasingly tend to arrive at the ROIC without being captured by the holes. This phenomenon is called “electron trapping.” The time-variation component due to the

electron trapping can be reduced down to several hundred ppm by preflashing, which irradiates the detector plane with bright stellar light before transit observations, such that the holes are buried by the photoelectrons generated due to the bright object (Knutson et al. 2009; Seager & Deming 2009). Regarding the fallback after the steep ramp, although what is behind the fallback is still unknown, the fallback may be related to the persistent effect in the multiplexers of the ROIC (Crossfield et al. 2012). Note that there are some cases where no ramp and fallback are observed in the transit phase curve (e.g., Knutson et al. 2007). The latent effect also leads to a potential systematic error. When a bright source is observed, it leaves its footprint on the detector even after it is removed. A latent level of about 1% for the bright source was reported for the detector systems developed for the mid-infrared instrument (MIRI) of the *JWST* (Ressler et al. 2015). Although the cause of the latent image is not fully understood, the latent effect is thought to be generated by capturing photoelectrons in the blocking layer of the semiconductor device and dielectric relaxation because of its long RC (resistor–capacitor) time constant, which is the time required to charge the circuit capacitor through the circuit resistance. (Rieke et al. 2015). The third systematic error arises from fluctuations of the bias voltage acting on the semiconductor and the constant voltages acting on the multiplexers of the ROIC. This occurs because the detector responsivity strongly depends on the bias voltage (Rieke et al. 2015), and the fluctuation of the constant voltages leads to the gain variation in the ROIC. Since a source follower is installed in each pixel unit of the complementary metal oxide semiconductor (CMOS) infrared detector system, there are individual noises that depend upon the pixels. Additionally, because the bias voltages are applied to every four pixels for the Si:As detectors developed for *JWST/MIRI*, gain variations are induced in the pixels and lead to pixel-to-pixel time variation if the bias voltages themselves vary in time. On the other hand, when time variation of the bias voltage exceeds the full-frame readout time, the temporal change in the bias voltage commonly affects the signals of all pixels. Therefore, high-frequency fluctuation of the bias voltage causes the gain variation between the pixels, and the common time variation of the gain over the entire detector occurs due to the low-frequency fluctuation. Note that, although the fluctuation in the low frequency is observed in the output signal as $1/f$ noise, it is difficult to perfectly separate the detector noise from the astronomical signal (Robberto 2014; Rauscher 2015).

Based on the above background, we propose a new method for correction of the time variation present in the semiconductor devices and ROIC, developing densified pupil spectroscopy. First, the light from an object is dispersed into a number of spectra by the densified pupil spectrograph, and a large number of pixels are exposed by the object light. The exposed pixels are named “science pixels.” The pixel-to-pixel time-variation components are smoothed out through the average of the science pixels, and the common components over the entire detector are extracted. Second, because the number of photons falling on a pixel is largely reduced, the steep ramp at the beginning of the transit observation can be mitigated if the ramp is caused due to electron trapping (e.g., Young et al. 2003; Crossfield et al. 2012). The latent effect can also be reduced owing to a small number of photoelectrons. Third, we place a cold photon-shield mask on which the densified subpupils are formed to block any thermal light. A number of

the cold pixels, in which only the dark current generates, are produced. We refer to the cold pixels as “reference pixels.” Since the value of the dark current is accurately proportional to the temperature of the detector (e.g., Ennico et al. 2003), the fluctuations of the reference pixels reflect the time variation generated in the detector system if the detector temperature is stable over the transit observation. Owing to the extraction of the common time-variation components over the entire detector by each average of the science and reference pixels, the long-term fluctuations acting on the science pixels can be calibrated by simultaneous measurement of the object and the reference signals. Note that several methods for calibration of the gain fluctuation with reference pixels, which are not sensitive to an object’s light and are different from those introduced in this paper, have been proposed (e.g., Rauscher et al. 2017; Rieke 2007).

In this paper, we propose a concept that mitigates and calibrates the systematic noises present in the mid-infrared wavelength range of detector systems used to characterize nearby transiting terrestrial planets. We briefly introduce the method for calibration of the systematic components and an optical design that enables the application of the calibration technique to spectrophotometric data in Section 2. Next, we describe the detailed analytical expression for the mid-infrared detector systems in Section 3. Assuming that the densified pupil spectrograph with the mid-infrared detector system is applied to the *Origins Space Telescope* (Fortney et al. 2018), we perform numerical simulations and show the results in Section 4. Finally, we raise several potential problems that are not considered in the numerical simulations and discuss the impacts on transit spectroscopy in Section 5.

2. Concept

In this section, we introduce a conceptual design for the calibration of the time-variation components present in a detector system composed of a semiconductor device and an ROIC, developing the densified pupil spectrograph. We also express the time-variation components with simple equations and show how the observational data acquired through the new design are calibrated and approach a true astronomical value that is free from the systematic components.

2.1. Design

When the numbers of the photons from an astronomical source and a background component, f_s and f_z , respectively, fall on an (i, j) pixel in a detector system with a quantum efficiency of η and a dark current corresponding to the number of electrons Q , the observational data D for the (i, j) pixel is written as a function of time t ,

$$D_{ij}(t) = A_{ij}(t)\beta(t, f_{ij})[\eta_{ij}\{\alpha'_{ij}(\text{WFE}(t))f_{s,ij}(t) + \alpha_{ij}f_{z,ij}\} + Q_{ij}] + V_{ij}, \quad (1)$$

where A is an effective gain that yields a conversion factor from electron to voltage (gain) in the detector system, β is another effective gain that indicates the fraction of the photoelectrons arriving at the ROIC to those generated in the semiconductor device, and α' and α are the effective gains for a point source and diffuse background, respectively. While the former effective pixel gains are determined by both the WFE in the optical system and intra- and interpixel sensitivity variation

(e.g., Barron et al. 2007; Carey et al. 2014), the latter is characterized by only the interpixel map. Here V is an offset voltage present in the readout electronics. Most of the factors shown in Equation (1) include time variation, as well as random components. The time variation of the effective gain, A , is caused by fluctuations of the bias voltage supplied to the semiconductor device and the constant voltages supplied to the ROIC. For detectors without a global shutter, such as the MIRI detectors developed for the *JWST*, while the high-frequency fluctuation produces pixel-to-pixel time variations, the low-frequency one leads to a common time variation over the entire detector. This is because the high-frequency fluctuation of the bias voltage leads to a different voltage being applied to each pixel, while the low-frequency fluctuation provides a constant voltage over the entire detector. Another effective gain, β , introduces a ramp at the beginning of the transit observation and a fallback over a timescale of 10–20 hr after the ramp, both of which are thought to be caused by the trapping of photoelectrons at holes due to detector impurities and the persistence effect of the ROIC. The effective pixel gains for a point source, α' , also contribute to the photometric variation because the WFE in the telescope and optical system leads to image movement and deformation on the intra- and interpixel variation. In the mid-infrared wavelength region, the zodiacal light contributes to the transit light curve as an offset component, as well as photon noise. Note that we assume that there is no variation of the background light from the zodiacal light during the transit observation. We also assume that Q is a constant dark current and V is reduced to random readout noise by a sophisticated detector sampling, such as correlated double sampling (CDS) and Fowler sampling (Vincent et al. 2016). Thus, the transit light curve related to $f(t)$ is mainly affected by the time variations of the two effective gains, $A(t)$ and $\beta(t)$; the effective pixel gain, α ; and the background component f_z for general-purpose spectrographs.

Here we propose a design for minimizing and calibrating the various time-variation components shown in Equation (1), developing the densified pupil spectroscopy concept that forms multiple spectra on the detector plane optically conjugated to the primary mirror of a telescope (Matsuo et al. 2016; see also Figure 2). First, because the densified pupil spectrograph provides the spectra of the divided primary mirror, the WFE present in the telescope and optical system does not lead to the image movement and deformation of the detector plane; therefore, $\alpha'(\text{WFE})$ for a point source becomes equal to that for a diffuse background, α . Second, owing to the multiple spectra formed on the number of the pixels, the pixel-to-pixel time-variation components with high frequency can be smoothed out through the average of the science pixels that are exposed by the object spectra. According to the transit spectrograph designed for the *Origins Space Telescope* (Matsuo et al. 2018), the number of samplings for each spectral element with a spectral resolution of 100 is around 2000. Thus, the common long-term variation in the entire detector is extracted from the averaged spectrum. Last, since the number of photons falling on each science pixel decreases, the timescale of the electron trapping decrease is much longer than that for a conventional spectrograph; hence, the long-term variation component due to the trapping effect can be

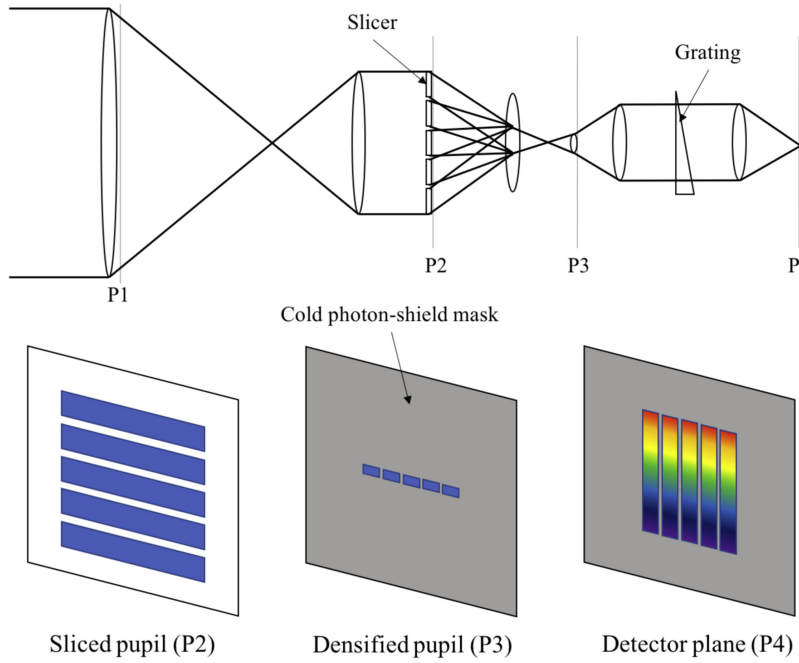


Figure 1. Conceptual design of the densified pupil spectrograph (top). The P1 plane is the primary mirror of a telescope, and the P2, P3, and P4 planes correspond to the pupil that is optically conjugated to the primary mirror P1. Incident light is first divided with a pupil slicer on the P2 plane. After that, the divided subpupils are rearranged in line, and each subpupil is densified on the P3 plane. The densified subpupils are diffracted as a point source and then dispersed with a diffraction grating. The spectra of the subpupils are formed on the detector plane P4.

approximately ignored. Note that we quantitatively evaluate the impact of the trapping effect on the transit spectroscopy in Section 5. Based on the above considerations, Equation (1), under the densified pupil spectrograph, is rewritten as

$$D_{ij}(t) \approx A_{ij}(t)[\alpha_{ij}\eta_{ij}\{f_s(t) + f_z\} + Q_{ij}] + \sigma_{\text{read},ij}, \quad (2)$$

where $\alpha'_{ij}(\text{WFE}(t))$ becomes α_{ij} for the densified pupil spectrograph, and $\sigma_{\text{read},ij}$ is the readout noise generated through the reduction of the offset voltage with CDS or Fowler sampling. In addition, the numbers of photons from the target object and background component, $f_{s,ij}(t)$ and $f_{z,ij}$, are replaced by $f_s(t)$ and f_z , respectively, which do not depend on the detector pixels exposed by the object light because the densified pupil spectrograph provides multiple equivalent rectangular spectra. The averaged signal over the science pixels is

$$\langle D_{ij}(t) \rangle_{\text{pix}} \approx A_{\text{com}}(t)[\langle \alpha_{ij}\eta_{ij} \rangle_{\text{pix}}\{f_s(t) + f_z\} + \langle Q_{ij} \rangle_{\text{pix}}] + \sqrt{\langle \sigma_{\text{read},ij}^2 \rangle_{\text{pix}}}, \quad (3)$$

where $\langle X \rangle_y$ indicates the averaged X over y and A_{com} represents the common time-variation gain over the entire detector, $\langle A_{ij}(t) \rangle_{\text{pix}} = A_{\text{com}}(t)$. Thus, when the densified pupil spectrograph is applied to the transit observations, the common low-frequency time-variation components, A_{com} , impact the transit light curve and the background light, f_z , and the dark current, Q , respectively.

In addition to the pixels exposed by the target light (i.e., science pixels), two types of pixels are prepared for calibration of the time-variation components and subtraction of the offset component. One is referred to as the “reference pixel,” which is generated by placing a photon-shield mask on a pupil plane (Figure 1, P3) to block any thermal light and in which only

dark current is generated. As discussed in the next section, because the dark current is also affected by the common time-variation components over the entire detector, the low-frequency systematic component can be reconstructed from the reference pixels. The other is called the “background pixel.” The observational field includes not only the host star and planet but also the background light (Figure 2(a)). Because the zodiacal light is very bright over the entire sky in the mid-infrared wavelength (e.g., Kelsall et al. 1998; Kondo et al. 2016), the zodiacal light contributes to the transit signal as an offset, as well as photon noise. In order to remove the background component, the two diffraction gratings on the focal plane are used and tilted differently so that the sum of the target and background light, and only the background light, are focused at two different positions on the detector plane (see Figure 2(b)). The background pixels are distributed over the same area as the science ones (Figure 2(c)).

There is an uncommon path error between the science and background pixels, which may affect the subtraction of the offset component from the science pixels. However, the individual difference of the two gratings can be ignored because the large-diameter science light enters the two gratings owing to the densified pupil spectrograph, leading to the local difference between the two gratings being smoothed out. In addition, even though the second grating is tilted relative to the astronomical light, the characteristic of the densified pupil spectroscopy remains; the noise floor of the background light is the same as that of the science light. On the other hand, because the background light is formed at the different locations on the detector plane, the flat-field error affects the zodiacal light differently from how it influences the science light. One possible way to mitigate the impact of the flat-field error on the proposed method is to observe only the zodiacal light with both

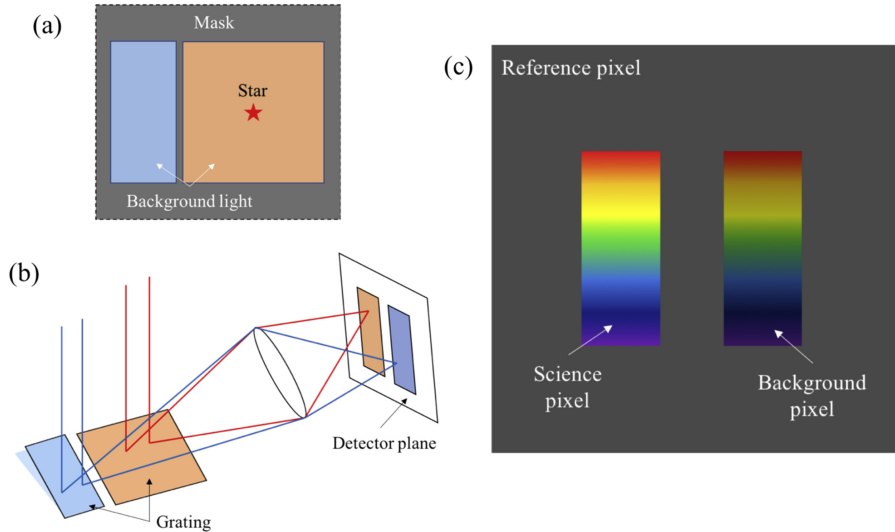


Figure 2. (a) Orange and blue regions indicate the two fields of view corresponding to the science pixels and background pixels, respectively. (b) Conceptual design of two diffraction gratings placed on the focal plane. (c) Example of pixel mapping on the detector plane for the modified design of the densified pupil spectrograph. There are three types of pixels: science pixels (bright rainbow), background pixels (dark rainbow), and reference pixels (black). The horizontal and vertical directions correspond to the spatial position of the pupil and the wavelength dispersion, respectively. The numbers of science and background pixels are equal and determined by the number of pupil slicers and the densification factor of the pupil size.

the science and background pixels and calibrate the difference between them before the science observations. Even if the residual offsets remain through the calibration, they can be eliminated by extracting the spectrum of the transiting planetary atmosphere (i.e., subtraction of the signal before and after the transit from that during the transit). This is because the residual offset is not expected to change over a single transit observation. Note that we quantitatively discuss the impact of the flat-field uncertainty upon the proposed method in Section 4.

2.2. Method

We briefly introduce the procedure for the proposed method in this subsection. The reference and background pixels that are generated by the modified design of the densified pupil spectrograph are applied for calibration of the systematic components present in the semiconductor device and ROIC. The signals of the science, background, and reference pixels, $D_{\text{sci},ij}$, $D_{\text{back},ij}$, and $D_{\text{ref},ij}$, are, respectively, written as

$$D_{\text{sci},ij}(t) \approx A_{ij}(t)[\alpha_{ij}\eta_{ij}\{f_s(t) + f_z\} + Q_{ij}] + \sigma_{\text{read},ij}, \quad (4)$$

$$D_{\text{back},ij}(t) \approx A_{ij}(t)(\alpha_{ij}\eta_{ij}f_z + Q_{ij}) + \sigma_{\text{read},ij}, \quad (5)$$

and

$$D_{\text{ref},ij}(t) \approx A_{ij}(t)Q_{ij} + \sigma_{\text{read},ij}. \quad (6)$$

We average the signals over these pixels to smooth out the pixel-to-pixel variations (process I). An overview of the method for calibration of gain variation in the detector system is shown in Figure 3. Subsequently, the calibration of the common time-variation component is implemented using the reference and background pixels. Since the time-variation component is common to all of the detector pixels, including the reference and background pixels, as well as the science pixels, it is possible to reconstruct the common systematic

components from the reference and background data because the reference and background pixels are not affected by the transit signal but by the common systematic components. The systematic components associated with the reference and background data are derived by subtraction of the time- and pixel-averaged ones from the pixel-averaged ones at each frame. Given that there is linearity among the three types of pixels, the calibrated signal, D_{cal} , is acquired by subtraction of the common time-fluctuation components without a transit signal from the average value over the science pixel (process II). Last, using the time- and pixel-averaged background pixel value, the offset component can also be subtracted; D_{sub} is acquired (process III), and we can obtain the normalized transit signal, $D_{\text{sub,norm}}$, using the subtracted data (process IV). Thus, we can obtain the calibrated signal that is free from both the systematic and offset components. Note that we assumed the dark current and background light to be constant during the transit observation. The proposed method requires stabilization of the detector's temperature and calibration of the dark current value using the time series of the detector temperature. On the other hand, we also discuss cases where the dark current and zodiacal light have time-variation fluctuations and evaluate how the time-variation components of the dark current and zodiacal light affect the proposed method in Section 5.2. In Section 3, we show a detailed mathematical description of the conceptual design optimized for CMOS infrared detector systems.

3. Mathematical Analysis for Infrared Detector Systems

In this section, we apply the proposed method for calibration of the long-term variation components to infrared detector systems and show a mathematical description of the method optimized for the infrared detector systems. In this paper, we

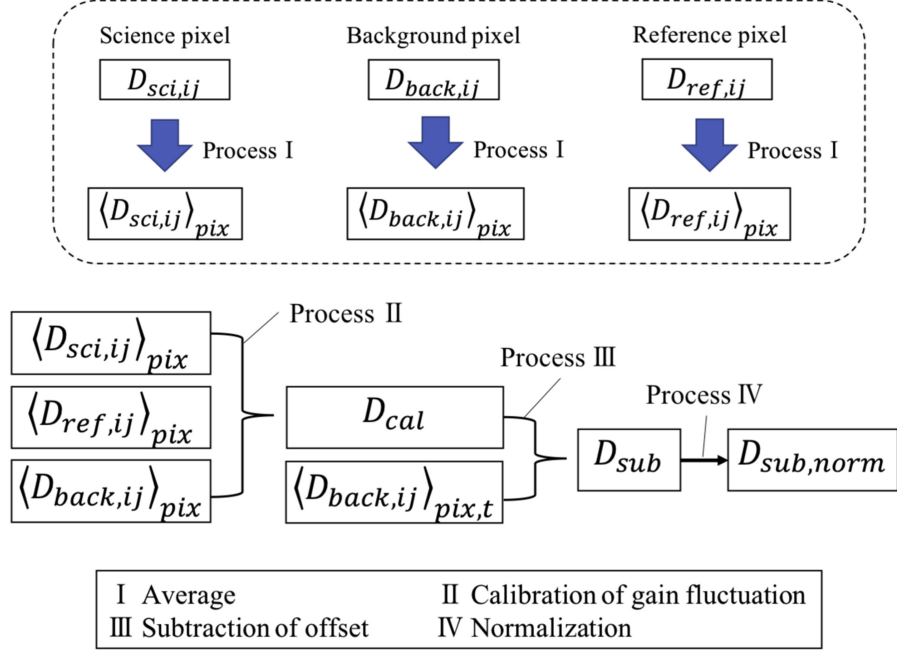


Figure 3. Flowchart of the calibration method.

refer to papers on the detector sampling and ROIC developed for the infrared detector systems (Johnson & Lomheim 2009; Ressler et al. 2015).

The detector system operating in the infrared wavelength range is mainly divided into three subsystems: a semiconductor device, in which photons enter and are converted to photoelectrons; an ROIC, in which the photoelectrons are converted to voltage in each pixel unit and voltages of all of the detector pixels are combined into one or a few signal lines through one or more multiplexers; and several noncryogenic electronics, in which the combined voltages are transferred to digital values with analog-to-digital converters (ADCs). The CDS and Fowler sampling are done in the software to reduce the offset voltage into random noise. This paper focuses on the former two subsystems, which mainly cause the time-variation components among the three subsystems. The parameters and symbols used for the mathematical analysis in Section 3 are compiled in the table of the Appendix.

3.1. Formulation of Output Voltage

We first formulate the output voltage at the k th readout gate of the ROIC in the infrared detector. Figure 4 shows an equivalent circuit of the ROIC (Johnson & Lomheim 2009) and the signal flow from receiving photons on the detector plane to sending voltages converted from photoelectrons to the warm electronics. The signal flow from the semiconductor device to the gate of the ROIC is mainly divided into three parts. First, the photoelectrons and electrons corresponding to dark current are converted into voltage in each pixel unit through the charging of the electrons at its condenser. Note that the electrons are integrated at the gate of the source follower in each unit cell for the MIRI detector developed for the *JWST*. When the number of photons per second f_{ij} at the observing wavelength λ falls on the (i, j) detector pixel and the generated

electrons are accumulated at the condenser during the exposure time t_{exp} , the output voltage at the gate of the source follower in each unit cell $v_{\text{int},ij}$ is written as

$$v_{\text{int},ij}(\lambda, t) \approx \frac{\alpha_{ij}\eta_{ij}f_{ij}(\lambda, t) + I_{\text{dark},ij}}{C_{ij}}t_{\text{exp}} + V_{\text{res},ij}, \quad (7)$$

where C_{ij} is the capacitor capacitance of the (i, j) pixel, $I_{\text{dark},ij}$ is the dark current in the (i, j) pixel, and $V_{\text{res},ij}$ is the offset voltage generated when resetting the electrons accumulated at the condenser of the (i, j) pixel. Next, the voltage is transferred to the column multiplexer through the source follower of each pixel and to the source follower at each readout gate of the ROIC. The output voltage at the readout gate $v_{\text{out},ijk}$ is

$$v_{\text{out},ijk}(\lambda, t) \approx A_k(t)A_{ij}(t)\gamma_{ij}\{\alpha_{ij}\eta_{ij}f_{ij}(\lambda, t) + I_{\text{dark},ij}\}, \quad (8)$$

where A_{ij} and A_k are the transfer function of the source follower in the (i, j) pixel and at the k th readout gate, respectively, and $\gamma_{ij} \equiv t_{\text{exp}}/C_{ij}$. Note that, although v_{out} is generally calculated as a convolution of A_{ij} , A_k , and $\gamma_{ij}\{\alpha_{ij}\eta_{ij}f_{ij}(\lambda, t) + I_{\text{dark},ij}\}$, the convolution is approximately replaced by multiplication because the source followers applied to the astronomical detectors have wide bandwidths (Johnson 1999; Johnson & Lomheim 2009). The $V_{\text{res},ij}$ present in Equation (7) can be reduced to a random component with CDS or Fowler sampling in the software. Thus, the transit signal is mostly affected by the time variations of the two effective gains multiplied with $f_{ij}(\lambda, t)$. The offset voltage, however, is present in the multiplexer of ROIC; its impact on the transit signal is evaluated in Section 5.

3.2. Output Voltages for Three Types of Pixels

We apply the densified pupil spectrograph to the infrared detector system and then formulate the output voltages at the

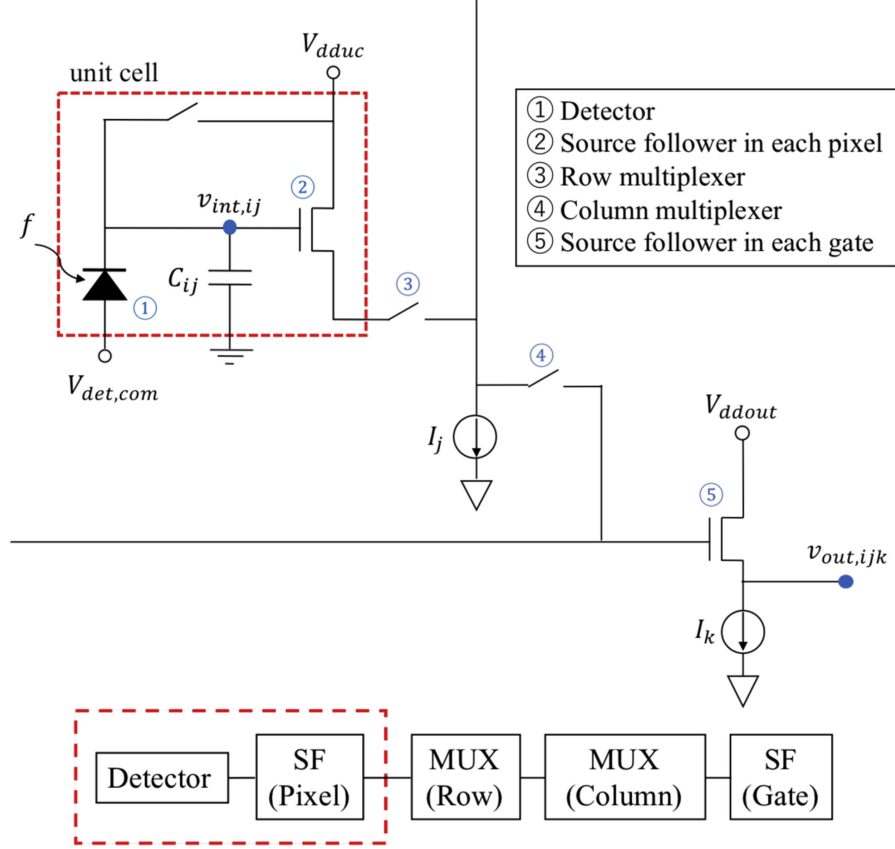


Figure 4. Equivalent circuit of an infrared detector system (top) and flowchart of its signal chain (bottom).

kth readout gate for the three types of pixels: the science, background, and reference pixels. In analogy with the mathematical analysis introduced in Section 2.2, the voltage at the k th readout gate of ROIC is decomposed into the sum of the average, fluctuation, and random terms of $v_{out,ijk}$,

$$v_{out,ijk}(\lambda, t) = \langle v_{out,ijk}(\lambda, t) \rangle_t + \delta v_{out,ijk}(\lambda, t) + \sigma_{out,ijk}(\lambda), \quad (9)$$

where $\langle v_{out,ijk}(\lambda, t) \rangle_t$ is the time average of $v_{out,ijk}(\lambda, t)$ over one transit observation, $\delta v_{out,ijk}(\lambda, t)$ is the time variation of $v_{out,ijk}(\lambda, t)$, and $\sigma_{out,ijk}(\lambda)$ is the random components associated with $v_{out,ijk}(\lambda, t)$. The time-averaged values of the science, background, and reference pixels, $\langle v_{sci,ijk}(\lambda, t) \rangle_t$, $\langle v_{back,ijk}(\lambda, t) \rangle_t$, and $\langle v_{ref,ijk}(t) \rangle_t$, are

$$\begin{aligned} \langle v_{sci,ijk}(\lambda, t) \rangle_t &\approx \langle A_k(t) \rangle_t \langle A_{ij}(t) \rangle_t \gamma_{ij} \\ &\times [\alpha_{ij} \eta_{ij} \{ \langle f_s(\lambda, t) \rangle_t + f_z(\lambda) \} + I_{dark,ij}], \end{aligned} \quad (10)$$

$$\begin{aligned} \langle v_{back,ijk}(\lambda, t) \rangle_t &\approx \langle A_k(t) \rangle_t \langle A_{ij}(t) \rangle_t \gamma_{ij} \\ &\times \{ \alpha_{ij} \eta_{ij} f_z(\lambda) + I_{dark,ij} \}, \end{aligned} \quad (11)$$

and

$$\langle v_{ref,ijk}(t) \rangle_t \approx \langle A_k(t) \rangle_t \langle A_{ij}(t) \rangle_t \gamma_{ij} I_{dark,ij}, \quad (12)$$

where f_s and f_z are the numbers of photons from a target object and the zodiacal light falling on a detector pixel, respectively.

Given that more than second-order fluctuations are ignored and the variation of the zodiacal light δf_z is much smaller than the transit signal δf_s , the time-variation terms in Equation (9) for the three types of pixels, $\delta v_{sci,ijk}$, $\delta v_{back,ijk}$, and $\delta v_{ref,ijk}$, become

$$\begin{aligned} \delta v_{sci,ijk}(\lambda, t) &\approx \langle A_k(t) \rangle_t \langle A_{ij}(t) \rangle_t \gamma_{ij} \alpha_{ij} \eta_{ij} \delta f_s(\lambda, t) \\ &+ \langle A_{ij}(t) \rangle_t \gamma_{ij} [\alpha_{ij} \eta_{ij} \{ \langle f_s(\lambda, t) \rangle_t + f_z(\lambda) \} \\ &+ I_{dark,ij}] \delta A_k(t) \\ &+ \langle A_k(t) \rangle_t \gamma_{ij} [\alpha_{ij} \eta_{ij} \{ \langle f_s(\lambda, t) \rangle_t + f_z(\lambda) \} \\ &+ I_{dark,ij}] \delta A_{ij}(t), \end{aligned} \quad (13)$$

$$\begin{aligned} \delta v_{back,ijk}(\lambda, t) &\approx \langle A_{ij}(t) \rangle_t \gamma_{ij} \{ \alpha_{ij} \eta_{ij} f_z(\lambda) \\ &+ I_{dark,ij} \} \delta A_k(t) \\ &+ \langle A_k(t) \rangle_t \gamma_{ij} \{ \alpha_{ij} \eta_{ij} f_z(\lambda) + I_{dark,ij} \} \delta A_{ij}(t), \end{aligned} \quad (14)$$

and

$$\begin{aligned} \delta v_{ref,ijk}(t) &\approx \langle A_{ij}(t) \rangle_t \gamma_{ij} I_{dark,ij} \delta A_k(t) \\ &+ \langle A_k(t) \rangle_t \gamma_{ij} I_{dark,ij} \delta A_{ij}(t). \end{aligned} \quad (15)$$

The terms δA_{ij} and δA_k in Equations (13)–(15) correspond to the systematic components that have an impact on the transit light curve. Considering each random component is statistically independent, the random noise acting on the three types of pixels, $\sigma_{sci,ijk}$, $\sigma_{back,ijk}$, and $\sigma_{ref,ijk}$, can be written as

$$\sigma_{\text{sci},ijk}(\lambda) \approx \sqrt{\langle A_k(t) \rangle_t^2 \langle A_{ij}(t) \rangle_t^2 \gamma_{ij}^2 [\alpha_{ij}^2 \eta_{ij}^2 \{\sigma_{\text{photon},s}^2(\lambda) + \sigma_{\text{photon},z}^2(\lambda)\} + \sigma_{\text{dark},ij}^2] + \sigma_{\text{read},ijk}^2}, \quad (16)$$

$$\begin{aligned} \sigma_{\text{back},ijk}(\lambda) \\ \approx \sqrt{\langle A_k(t) \rangle_t^2 \langle A_{ij}(t) \rangle_t^2 \gamma_{ij}^2 [\alpha_{ij}^2 \eta_{ij}^2 \sigma_{\text{photon},z}^2(\lambda) + \sigma_{\text{dark},ij}^2] + \sigma_{\text{read},ijk}^2}, \end{aligned} \quad (17)$$

and

$$\sigma_{\text{ref},ijk} \approx \sqrt{\langle A_k(t) \rangle_t^2 \langle A_{ij}(t) \rangle_t^2 \gamma_{ij}^2 \sigma_{\text{dark},ij}^2 + \sigma_{\text{read},ijk}^2}, \quad (18)$$

where $\sigma_{\text{photon},s}$, $\sigma_{\text{photon},z}$, and σ_{dark} are the shot noise of the object light, zodiacal light, and dark current, respectively.

3.3. Calibration Process

We optimize the calibration method introduced in Section 2.2 for the infrared detector systems and mathematically show how to calibrate the time-variation components with the three types of pixels. The process of the calibration method is mainly divided into four steps. The first step of the calibration is to average the pixel values over all the pixels exposed by the same spectrally resolved light for the science and background pixels $v_{\text{sci},ijk}(\lambda, t)$ and $v_{\text{back},ijk}(\lambda, t)$, as well as for those over all the reference pixels, $v_{\text{ref},ijk}(t)$, to smooth out pixel-to-pixel time variations and extract the common systematic components of all of the pixels. The pixel-averaged science and background values are

$$\begin{aligned} \langle v_{\text{sci},ij}(\lambda, t) \rangle_{\text{pix}} &= \frac{\sum_{ijk} v_{\text{sci},ijk}(\lambda, t)}{n_{\text{sci}}(\lambda)} = \frac{\sum_{ijk} \langle v_{\text{sci},ijk}(\lambda, t) \rangle_t}{n_{\text{sci}}(\lambda)} \\ &+ \frac{\sum_{ijk} \delta v_{\text{sci},ijk}(\lambda, t)}{n_{\text{sci}}(\lambda)} + \frac{\sqrt{\sum_{ijk} \sigma_{\text{sci},ijk}^2(\lambda)}}{n_{\text{sci}}(\lambda)}, \end{aligned} \quad (19)$$

$$\begin{aligned} \langle v_{\text{back},ij}(\lambda, t) \rangle_{\text{pix}} &= \frac{\sum_{ijk} v_{\text{back},ijk}(\lambda, t)}{n_{\text{back}}(\lambda)} = \frac{\sum_{ijk} \langle v_{\text{back},ijk}(\lambda, t) \rangle_t}{n_{\text{back}}(\lambda)} \\ &+ \frac{\sum_{ijk} \delta v_{\text{back},ijk}(\lambda, t)}{n_{\text{back}}(\lambda)} + \frac{\sqrt{\sum_{ijk} \sigma_{\text{back},ijk}^2(\lambda)}}{n_{\text{back}}(\lambda)}, \end{aligned} \quad (20)$$

where $n_{\text{sci}}(\lambda)$ and $n_{\text{back}}(\lambda)$ are the numbers of science and background pixels exposed by the same component of λ . The

pixel-averaged value over the reference pixels becomes

$$\begin{aligned} \langle v_{\text{ref},ij}(t) \rangle_{\text{pix}} &= \frac{\sum_{ijk} v_{\text{ref},ijk}(t)}{n_{\text{ref}}} = \frac{\sum_{ijk} \langle v_{\text{ref},ijk}(t) \rangle_t}{n_{\text{ref}}} \\ &+ \frac{\sum_{ijk} \delta v_{\text{ref},ijk}(t)}{n_{\text{ref}}} + \frac{\sqrt{\sum_{ijk} \sigma_{\text{ref},ijk}^2}}{n_{\text{ref}}}, \end{aligned} \quad (21)$$

where n_{ref} is the number of reference pixels. Using Equations (10)–(15), Equations (19)–(21) become

$$\begin{aligned} \langle v_{\text{sci},ij}(\lambda, t) \rangle_{\text{pix}} &= \langle A_{\text{com}}(t) \rangle_t \langle \gamma_{ij} \rangle_{\text{pix}} \\ &\times [\langle \alpha_{ij} \eta_{ij} \rangle_{\text{pix}} \{ \langle f_s(\lambda, t) \rangle_t + f_z(\lambda) \} \\ &+ \langle I_{\text{dark},ij} \rangle_{\text{pix}}] \\ &+ \langle A_{\text{com}}(t) \rangle_t \langle \gamma_{ij} \rangle_{\text{pix}} \langle \alpha_{ij} \eta_{ij} \rangle_{\text{pix}} \delta f_s(\lambda, t) \\ &+ \langle \gamma_{ij} \rangle_{\text{pix}} [\langle \alpha_{ij} \eta_{ij} \rangle_{\text{pix}} \{ \langle f_s(\lambda, t) \rangle_t + f_z(\lambda) \} \\ &+ \langle I_{\text{dark},ij} \rangle_{\text{pix}}] \delta A_{\text{com}}(t) + \sqrt{\langle \sigma_{\text{sci},ij}^2(\lambda) \rangle_{\text{pix}}} \\ &+ \sqrt{\langle \sigma_{\text{sci},ij}^2(\lambda) \rangle_{\text{pix}}} \frac{\delta A_{\text{com}}(t)}{\langle A_{\text{com}}(t) \rangle_t}, \end{aligned} \quad (22)$$

$$\begin{aligned} \langle v_{\text{back},ij}(\lambda, t) \rangle_{\text{pix}} &= \langle A_{\text{com}}(t) \rangle_t \langle \gamma_{ij} \rangle_{\text{pix}} \\ &\times \{ \langle \alpha_{ij} \eta_{ij} \rangle_{\text{pix}} f_z(\lambda) + \langle I_{\text{dark},ij} \rangle_{\text{pix}} \} \\ &+ \langle \gamma_{ij} \rangle_{\text{pix}} \{ \langle \alpha_{ij} \eta_{ij} \rangle_{\text{pix}} f_z(\lambda) \\ &+ \langle I_{\text{dark},ij} \rangle_{\text{pix}} \} \delta A_{\text{com}}(t) + \sqrt{\langle \sigma_{\text{back},ij}^2(\lambda) \rangle_{\text{pix}}} \\ &+ \sqrt{\langle \sigma_{\text{back},ij}^2(\lambda) \rangle_{\text{pix}}} \frac{\delta A_{\text{com}}(t)}{\langle A_{\text{com}}(t) \rangle_t}, \end{aligned} \quad (23)$$

$$\begin{aligned} \langle v_{\text{ref},ij}(t) \rangle_{\text{pix}} &= \langle A_{\text{com}}(t) \rangle_t \langle \gamma_{ij} \rangle_{\text{pix}} \langle I_{\text{dark},ij} \rangle_{\text{pix}} \\ &+ \langle \gamma_{ij} \rangle_{\text{pix}} \langle I_{\text{dark},ij} \rangle_{\text{pix}} \delta A_{\text{com}}(t) + \sqrt{\langle \sigma_{\text{ref},ij}^2 \rangle_{\text{pix}}} \\ &+ \sqrt{\langle \sigma_{\text{ref},ij}^2 \rangle_{\text{pix}}} \frac{\delta A_{\text{com}}(t)}{\langle A_{\text{com}}(t) \rangle_t}. \end{aligned} \quad (24)$$

The second step is to remove the time-variation components from the pixel-averaged science data using the pixel-averaged background and reference data. Focusing on the fact that the time-variation components associated with the background and reference data are composed of only the systematic components present in the semiconductor device and ROIC, as shown in Equations (14) and (15), the systematic components are derived by subtraction of the time- and pixel-averaged background and reference data over one transit observation, $\langle v_{\text{back},ij}(\lambda, t) \rangle_{\text{pix},t}$, $\langle v_{\text{ref},ij}(t) \rangle_{\text{pix},t}$, from the pixel-averaged background and

reference data, $\langle v_{\text{back},ij}(\lambda, t) \rangle_{\text{pix}}$, $\langle v_{\text{ref},ij}(t) \rangle_{\text{pix}}$, at each frame. Note that, because the amplitude of the time-variation component is proportional to the signal amplitude, the time-variation component associated with the science pixel can be reconstructed through multiplication of $\{\langle v_{\text{back},ij}(\lambda, t) \rangle_{\text{pix}} + \langle v_{\text{ref},ij}(t) \rangle_{\text{pix}}\} - \{\langle v_{\text{back},ij}(\lambda, t) \rangle_{\text{pix},t} + \langle v_{\text{ref},ij}(t) \rangle_{\text{pix},t}\}$ with the ratio of the time- and pixel-averaged science data to the sum of the background and reference data, $\frac{\langle v_{\text{sci},ij}(\lambda, t) \rangle_{\text{pix},t}}{\langle v_{\text{back},ij}(\lambda, t) \rangle_{\text{pix},t} + \langle v_{\text{ref},ij}(t) \rangle_{\text{pix},t}}$. Using Equations (22)–(24), the systematic component can be removed from the science data as follows:

$$\begin{aligned} v_{\text{cal}}(\lambda, t) &= \langle v_{\text{sci},ij}(\lambda, t) \rangle_{\text{pix}} - \{\langle v_{\text{back},ij}(\lambda, t) \rangle_{\text{pix}} \\ &\quad + \langle v_{\text{ref},ij}(t) \rangle_{\text{pix}}\} - \{\langle v_{\text{back},ij}(\lambda, t) \rangle_{\text{pix},t} \\ &\quad + \langle v_{\text{ref},ij}(t) \rangle_{\text{pix},t}\}] \\ &\quad \times \frac{\langle v_{\text{sci},ij}(\lambda, t) \rangle_{\text{pix},t}}{\langle v_{\text{back},ij}(\lambda, t) \rangle_{\text{pix},t} + \langle v_{\text{ref},ij}(t) \rangle_{\text{pix},t}} \\ &\approx \langle v_{\text{sci},ij}(\lambda, t) \rangle_{\text{pix},t} \\ &\quad + \langle A_{\text{com}}(t) \rangle_t \langle \gamma_{ij} \rangle_{\text{pix}} \langle \alpha_{ij} \eta_{ij} \rangle_{\text{pix}} \delta f_s(\lambda, t) \\ &\quad + \langle v_{\text{sci},ij}(\lambda, t) \rangle_{\text{pix},t} \frac{\delta A_{\text{com}}(t)}{\langle A_{\text{com}}(t) \rangle_t} \\ &\quad + \sqrt{\langle \sigma_{\text{sci},ij}^2(\lambda) \rangle_{\text{pix}}} + \sqrt{\langle \sigma_{\text{sci},ij}^2(\lambda) \rangle_{\text{pix}}} \frac{\delta A_{\text{com}}(t)}{\langle A_{\text{com}}(t) \rangle_t} \\ &\quad - [\{\langle v_{\text{back},ij}(\lambda, t) \rangle_{\text{pix},t} + \langle v_{\text{ref},ij}(t) \rangle_{\text{pix},t}\} \\ &\quad \times \frac{\delta A_{\text{com}}(t)}{\langle A_{\text{com}}(t) \rangle_t} \\ &\quad + \sqrt{\langle \sigma_{\text{back},ij}^2(\lambda) \rangle_{\text{pix}}} + \langle \sigma_{\text{ref},ij}^2 \rangle_{\text{pix}} \\ &\quad \times \left\{ 1 + \frac{\delta A_{\text{com}}(t)}{\langle A_{\text{com}}(t) \rangle_t} \right\} \\ &\quad \times \frac{\langle v_{\text{sci},ij}(\lambda, t) \rangle_{\text{pix},t}}{\langle v_{\text{back},ij}(\lambda, t) \rangle_{\text{pix},t} + \langle v_{\text{ref},ij}(t) \rangle_{\text{pix},t}} \\ &\approx \langle A_{\text{com}}(t) \rangle_t \langle \gamma_{ij} \rangle_{\text{pix}} [\langle \alpha_{ij} \eta_{ij} \rangle_{\text{pix}} \{\langle f_s(\lambda, t) \rangle_t \\ &\quad + f_z(\lambda)\} + \langle I_{\text{dark},ij} \rangle_{\text{pix}}] \\ &\quad + \langle A_{\text{com}}(t) \rangle_t \langle \gamma_{ij} \rangle_{\text{pix}} \langle \alpha_{ij} \eta_{ij} \rangle_{\text{pix}} \delta f_s(\lambda, t) \\ &\quad + \sigma_{\text{cal}}(\lambda) + \sigma_{\text{cal}}(\lambda) \frac{\delta A_{\text{com}}(t)}{\langle A_{\text{com}}(t) \rangle_t}, \end{aligned} \quad (25)$$

where $v_{\text{cal}}(\lambda, t)$ and $\sigma_{\text{cal}}(\lambda)$ are the calibrated science data and the random term associated with $v_{\text{cal}}(\lambda, t)$ after the second process, respectively. Note that the common systematic component can be reduced to a random one when the gain is perfectly proportional to various signal levels. The next step is to remove the offset component included in the science data reduced through the second step. Since the sum of the zodiacal

light and the dark current is equal to the time- and pixel-averaged value of the background pixels, the offset components can be removed through subtraction of $\langle v_{\text{back},ij}(\lambda, t) \rangle_{\text{pix},t}$ from $v_{\text{cal}}(\lambda, t)$:

$$\begin{aligned} v_{\text{sub}}(\lambda, t) &\approx v_{\text{cal}}(\lambda, t) - \langle v_{\text{back},ij}(\lambda, t) \rangle_{\text{pix},t} \\ &= \langle A_{\text{com}}(t) \rangle_t \langle \gamma_{ij} \rangle_{\text{pix}} [\langle \alpha_{ij} \eta_{ij} \rangle_{\text{pix}} \{\langle f_s(\lambda, t) \rangle_t \\ &\quad + f_z(\lambda)\} + \langle I_{\text{dark},ij} \rangle_{\text{pix}}] \\ &\quad + \langle A_{\text{com}}(t) \rangle_t \langle \gamma_{ij} \rangle_{\text{pix}} \langle \alpha_{ij} \eta_{ij} \rangle_{\text{pix}} \delta f_s(\lambda, t) \\ &\quad + \sigma_{\text{cal}}(\lambda) + \sigma_{\text{cal}}(\lambda) \frac{\delta A_{\text{com}}(t)}{\langle A_{\text{com}}(t) \rangle_t} \\ &\quad - \langle A_{\text{com}}(t) \rangle_t \langle \gamma_{ij} \rangle_{\text{pix}} \{\langle \alpha_{ij} \eta_{ij} \rangle_{\text{pix}} f_z(\lambda) \\ &\quad + \langle I_{\text{dark},ij} \rangle_{\text{pix}}\} \\ &= \langle A_{\text{com}}(t) \rangle_t \langle \gamma_{ij} \rangle_{\text{pix}} \langle \alpha_{ij} \eta_{ij} \rangle_{\text{pix}} \langle f_s(\lambda, t) \rangle_t \\ &\quad + \langle A_{\text{com}}(t) \rangle_t \langle \gamma_{ij} \rangle_{\text{pix}} \langle \alpha_{ij} \eta_{ij} \rangle_{\text{pix}} \delta f_s(\lambda, t) + \sigma_{\text{cal}}(\lambda) \\ &\quad + \sigma_{\text{cal}}(\lambda) \frac{\delta A_{\text{com}}(t)}{\langle A_{\text{com}}(t) \rangle_t}. \end{aligned} \quad (27)$$

Here the noise introduced during the subtraction is considered as negligible because the residual offset is not expected to change over a single transit observation. Last, we can obtain the normalized signal, $v_{\text{sub},\text{norm}}$, using the $v_{\text{sub}}(\lambda, t)$ of Equation (27),

$$v_{\text{sub},\text{norm}}(\lambda, t) \approx 1 + \frac{\delta f_s(\lambda, t)}{\langle f_s(\lambda, t) \rangle_t} + \sigma_{\text{sub},\text{norm}}(\lambda) + \Delta_{\text{sub},\text{norm}}(\lambda, t), \quad (28)$$

where $\sigma_{\text{sub},\text{norm}}(\lambda)$ and $\Delta_{\text{sub},\text{norm}}(\lambda, t)$ are the random and quadratic terms associated with $v_{\text{sub},\text{norm}}(\lambda, t)$:

$$\sigma_{\text{sub},\text{norm}}(\lambda) = \frac{\sigma_{\text{cal}}(\lambda)}{\langle A_{\text{com}}(t) \rangle_t \langle \gamma_{ij} \rangle_{\text{pix}} \langle \alpha_{ij} \eta_{ij} \rangle_{\text{pix}} \langle f_s(\lambda, t) \rangle_t}, \quad (29)$$

$$\begin{aligned} \Delta_{\text{sub},\text{norm}}(\lambda, t) &= \frac{\sigma_{\text{cal}}(\lambda)}{\langle A_{\text{com}}(t) \rangle_t \langle \gamma_{ij} \rangle_{\text{pix}} \langle \alpha_{ij} \eta_{ij} \rangle_{\text{pix}} \langle f_s(\lambda, t) \rangle_t} \\ &\quad \times \frac{\delta A_{\text{com}}(t)}{\langle A_{\text{com}}(t) \rangle_t} = \sigma_{\text{sub},\text{norm}}(\lambda) \frac{\delta A_{\text{com}}(t)}{\langle A_{\text{com}}(t) \rangle_t}. \end{aligned} \quad (30)$$

$$\sigma_{\text{cal}}(\lambda) = \sqrt{\left\langle \sigma_{\text{sci},ij}^2(\lambda) \right\rangle_{\text{pix}} + \left\{ \frac{\langle v_{\text{sci},ij}(\lambda, t) \rangle_{\text{pix},t}}{\langle v_{\text{back},ij}(\lambda, t) \rangle_{\text{pix},t} + \langle v_{\text{ref},ij}(t) \rangle_{\text{pix},t}} \right\}^2 \{\langle \sigma_{\text{back},ij}^2(\lambda) \rangle_{\text{pix}} + \langle \sigma_{\text{ref},ij}^2 \rangle_{\text{pix}}\}}, \quad (26)$$

As shown in Equation (30), when the gain variation, $\frac{\delta A_{\text{com}}}{\langle A_{\text{com}} \rangle_t}$, is small, the quadratic term, $\Delta_{\text{sub},\text{norm}}$, can be ignored. Thus, the systematic component common in the entire detector plane can be almost reduced to the random noise; however, the random noise obtained through the calibration process is larger than the one acting on the original science data, as shown in

Table 1
Characteristics of the Target Systems

Items	Case 1	Case 2	Case 3	Case 4
<i>Star</i>		...		
Distance (pc)	10	10	10	10
Effective temperature (K)	2500	3000	3500	4000
Radius (R_{\odot}) ^a	0.10	0.16	0.39	0.60
<i>Planet</i>		<i>Terrestrial Planet</i>		
Inclination (deg)	90	90	90	90
Albedo	0.31	0.31	0.31	0.31
Semimajor axis (10^{-3} au)	14.6	33.0	110.3	224.6
Period (days)	5.2	6.8	21.1	48.9
Equilibrium temperature (K)	288.2	288.2	288.2	288.2
Radius (R_{\oplus})	1	1	1	1
<i>Zodiacal Light</i>		...		
Level at 9 μm (MJy sr^{-1})	5	5	5	5
Effective temperature (K)	275	275	275	275
Spectrum	Blackbody	Blackbody	Blackbody	Blackbody

Note.

^a We cited Boyajian et al. (2012, 2017) and Mann et al. (2015) for the stellar radii of cases 2, 3, and 4. On the other hand, we referred to the stellar parameters of the Trappist-1 system (Gillon et al. 2017; Van Grootel et al. 2018) for the stellar radius of case 1.

Equation (29). As the integration time increases, $\sigma_{\text{sub,norm}}$ further decreases, and the transit signal can be more accurately measured.

4. Simulation

In this section, we perform numerical simulations to investigate how much the spectrophotometric stability of a densified pupil spectrograph optimized for the mid-infrared wavelength range can be improved with the proposed calibration method under a future large cryogenic telescope such as the *Origins Space Telescope* (Fortney et al. 2018).

4.1. Setup

We first introduce the appropriate assumptions to perform valid evaluations on the effectiveness of the calibration technique. Four cases were considered for the numerical simulations. The distances to all the target systems were fixed to 10 pc. The effective temperatures of the four host stars were set to 2500, 3000, 3500, and 4000 K. The stellar radii were 0.1, 0.16, 0.39, and 0.60 times the Sun radius, respectively. The four host stars approximately corresponded to late-M, mid-M, early-M, and late-K stars. Note that, since limb darkening has a small impact on the transit light curve in the mid-infrared wavelength range, no limb darkening was assumed to exist in the numerical simulations. The transiting planet orbiting each host star was assumed to be a terrestrial planet with a radius of 1 Earth radius and effective temperature of 288 K. Given that the albedos of the target planets were 0.306 and the inclinations were fixed to 90°, the semimajor axes of the planets were set to 0.015, 0.030, 0.110, and 0.225 au for the four simulation cases, respectively; the orbital periods were 5.2, 6.8, 21.1, and 48.9 days. The light from the target system was embedded in the

zodiacal light that was almost blackbody with an effective temperature of 275 K. Based on the previous observation (Kondo et al. 2016), the surface brightness of the zodiacal light was set to 5 MJy sr⁻¹ at 9 μm . The characteristics of the four target systems are compiled in Table 1.

The target systems were assumed to be observed with a large cryogenic space telescope such as the *Origins Space Telescope*. The primary mirror of the *Origins Space Telescope* is 9.24 m in diameter. The densified pupil spectrograph was applied to the transit observation. We assumed that the systematic components generated due to wavefront aberration in the telescope and instrument systems can be ignored because the system provides multiple spectra of the divided primary mirror on the detector plane. The transit instrument applies two mercury-cadmium-telluride (MCT) detectors (e.g., McMurtry et al. 2013) and one Si:As blocked-impurity-band (BIB) detector (e.g., Rieke et al. 2015; Ressler et al. 2015) to cover the wide wavelength range of 3–11 and 11–22 μm , respectively. The wavelength ranges of the spectra formed on the three detectors are 3–6, 6–11, and 11–22 μm , respectively. The pixel formats of the three detectors are 1024 × 1024. The numbers of science, background, and reference pixels for each detector were set to 120,000, 120,000, and 760,000, respectively. The field of view of the field stop used for this simulation was set to 2'' in radius, such that the photometric variation caused by the PSF motion loss on the field stop under a telescopic jitter of 10 mas was smaller than 1 ppm. Note that the PSF motion loss on the field stop can be calculated based on a mathematical formula introduced by Itoh et al. (2017). The optical throughput of the instrument, including the quantum efficiency of the detector, is 30% for each band. The minimum spectral-resolved wavelength, $\Delta\lambda$, was set to 0.01 times the central wavelength of each spectral channel—0.045 μm for the shorter band, 0.085 μm for the middle one, and 0.165 μm for the longer one—almost corresponding to the spectral resolution of 100 for the general-purpose spectrographs. Note that, while general-purpose spectrographs provide a constant $\lambda/\Delta\lambda$, $\Delta\lambda$ was fixed for the densified pupil spectral graph. The dark current of each detector was set to 1.0 $e^- \text{s}^{-1}$ for each band. The readout noise was set to approximately 5.5 e^- per read for both the MCT and Si:As detectors, assuming that CDS sampling and a Fowler-16 sampling were applied to the MCT and Si:As detectors, respectively (e.g., Rauscher et al. 2014; Rauscher 2015). The exposure time of each frame was set to 60 s for each simulation case, which is long enough that the dark current noise dominates the readout noise at one exposure for the reference pixels. Based on the flat-field uncertainty map derived from the *Wide-field Infrared Survey Explorer* (WISE) W3 data collected during the WISE cryogenic mission, the corrected effective gain after the flat-field calibration, corresponding to the conversion factor from electron to voltage, ranged from 0.99985 to 1.00015. Because the background and science spectra are focused at different locations on the detector plane, as shown in Figure 2, the subtraction of the background component from the object one cannot perfectly remove the offsets on the science data due to the flat-field uncertainty. Figure 5 shows the standard deviation of the systematic errors over the shorter wavelength of 3–22 μm generated by the subtraction of the background light as a function of the number of pixels for each spectral element. The flat-field uncertainty map of the WISE W3 data was used for this evaluation. As shown in Figure 5, the impact of the flat-

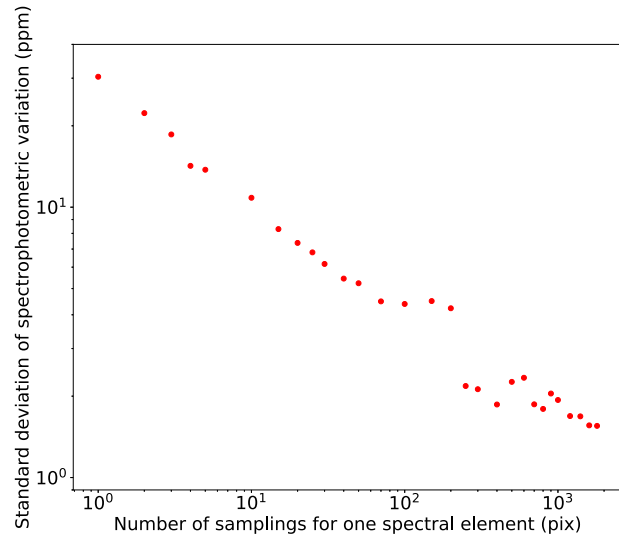


Figure 5. Standard deviation of spectrophotometric variation over the entire wavelength range of 3–22 μm as a function of the number of samplings for each spectral element. The effect of the uncertainty is reduced in proportion to the inverse of the square root of the number of pixels. Since the number of samplings is set to about 2000 pixels for this simulation, the flat-field uncertainty is negligible.

field uncertainty on this method is negligible, owing to the number of samplings for each spectral element. We also investigated whether the pixel-to-pixel time variation can be smoothed out through averaging the data. Figure 6 compares the science data with the reference set before and after the average without shot noise. The pixel-to-pixel time-variation components were almost smoothed out through the average, and the common components over the entire detector were extracted. Therefore, we assumed that the common components over the entire detector, A_{com} , remain in the transit light curve for this simulation. The standard deviation of the common component of the gain, $\sigma_{A_{\text{com}}}$, is set as

$$\sigma_{A_{\text{com}}} \equiv \sqrt{\int_{f_{\min}}^{f_{\max}} \sigma_g^2(f) df} = 1.0 \times 10^{-4}, \quad (31)$$

where σ_g is the standard deviation of the common component as a function of frequency, f , and is in inverse proportion to the rms of the frequency:

$$\sigma_g(f) \approx \frac{4.1 \times 10^{-5}}{\sqrt{f}}. \quad (32)$$

The frequencies of the common time-variation components range from 2×10^{-5} ($= f_{\min}$) to 8×10^{-3} ($= f_{\max}$) Hz. Based on the previous *Spitzer* observations (Knutson et al. 2009, 2011), the standard deviation of the time-variation components was set to 100 ppm. Note that the effective gain applied at the four readout gates ($k = 1, 2, 3$, and 4) A_k also remains because of the limited number of readout gates, which are four different effective gains, applied in this simulation. The offset estimation error is also negligible. The parameters of the telescope and the instrument are compiled in Table 2.

4.2. Results

We performed numerical simulations to investigate how much the systematic components are reduced with the calibration technique under the assumptions described in Section 4.1. The procedure for evaluation of the calibration method was as follows. First, a data set composed of 60 transit light curves, enabling acquisition with a sufficient signal-to-noise ratio to characterize the atmospheres of transiting Earth-size planets orbiting M-type stars, was generated for each simulation case, and the systematic components were reduced with the calibration method for each transit datum. The 60 calibrated transit light curves were coadded for reduction of random noise. For example, the signal-to-noise ratio for the late-M-type star was reduced to 25 ppm at 10 μm by coadding the 60 calibrated transit light curves. Figure 7 shows examples of the coadded transit light curves for the primary transits of transiting terrestrial planets orbiting the four host stars with different temperatures of 2500, 3000, 3500, and 4000 K. While the raw data for each simulation case (red points in Figure 7) are largely distorted by the systematic component, the calibrated data (cyan points) are randomly distributed around the input transit curve (black solid line). Figure 8 compares the histogram of the averaged calibration data at 10 μm over the 60 transit light curves with those of the averaged original and ideal data that include only shot noise for each simulation case. Although the calibration technique successfully removes the systematic components, the random error associated with the calibrated data is larger than that of the ideal data. This is because the calibrated data include not only the shot noise acting on the original science pixels but also the random errors of the background and reference pixels. The systematic and random errors for the coadded data were evaluated. The systematic error for each data set is defined as the residual between the depth of the model curve and that of the raw or calibrated data. The random error for each data set is defined as the rms of the two standard deviations for the transit and out-of-transit. Last, the above procedure was iterated 100 times, which enables us to derive the systematic error of the proposed method with an accuracy better than the standard deviation of the photon noise. Figure 9 shows the residuals between the input model curve and the raw or calibrated data for the four simulation cases. The residual of the raw data along the wavelength at each iteration has an offset value and is randomly distributed around the offset. In contrast, the residuals for the calibrated data sets are randomly distributed around zero, and the systematic components are successfully reduced to the random ones. Therefore, the standard deviation of the residuals for each wavelength is defined as the residual error of the calibrated simulation system. Figures 10 and 11 show the residual (systematic) and random errors in the wavelength range of 3–22 μm at primary and secondary eclipses for each simulation case, respectively. The residual errors for both the primary and secondary eclipses are almost the same; the calibration accuracy does not depend on the type of transit signal. In addition, the residual errors are almost consistent with the random ones of the raw data for cases 1–3 of this simulation because the calibrated data are free from the systematic components in these cases. As the effective temperature of the host star increases, the residual error can be further reduced. This occurs because the shot noise increases

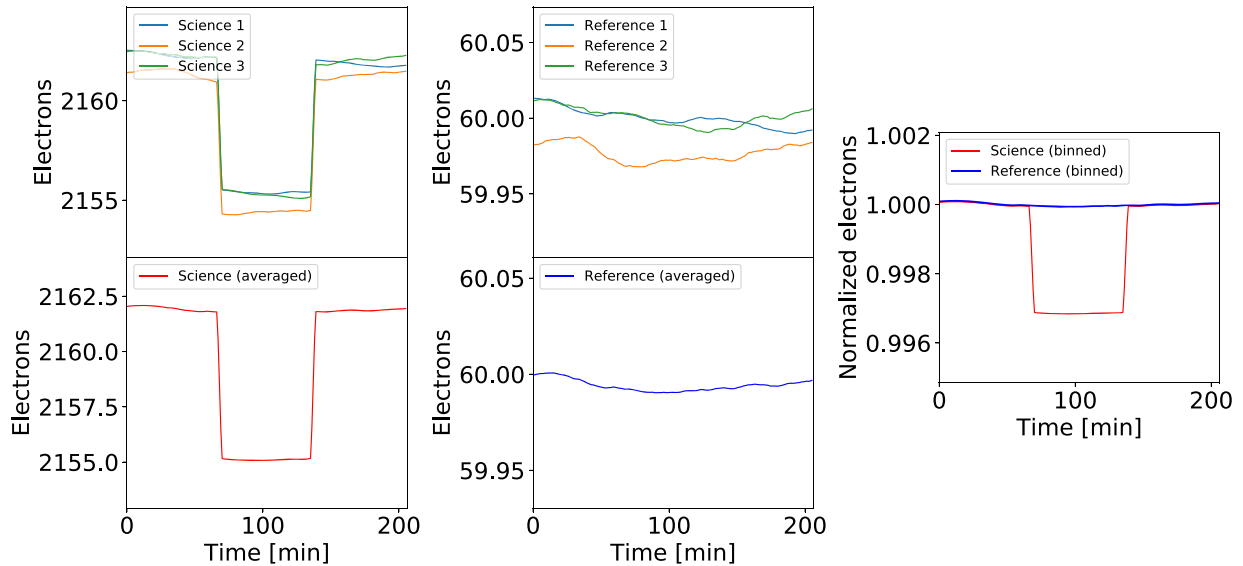


Figure 6. Comparison of the science pixel data with the reference pixel data without the shot noise. The blue, orange, and green lines in the upper left and right figures show three examples of data for the science and reference pixels. The lower left and right figures are the average data over the science and reference pixels, respectively. The pixel-to-pixel time variations of each data example are almost smoothed out. The right figure compares the averaged science data (red line) with the averaged reference data (blue line). The averaged reference data accurately trace the time-variation components associated with the science data.

Table 2

Specifications of the *Origin Space Telescope* and Its Transit Spectrograph

Items	Detector 1	Detector 2	Detector 3
<i>OST</i>			
Primary mirror diameter (cm)	924	924	924
<i>Transit Spectrograph</i>			
Detector type	MCT	MCT	Si:As
Pixel format	1024 × 1024	1024 × 1024	1024 × 1024
Number of science pixels	120,000	120,000	120,000
Number of background pixels	120,000	120,000	120,000
Number of reference pixels	760,000	760,000	760,000
Radius of field of view (arcsec)	2.0	2.0	2.0
Transmittance inc. QE (%)	30	30	30
Range of wavelength (μm)	3–6	6–11	11–22
Spectral resolution ($\lambda/\Delta\lambda$)	100	100	100
Exposure time at each frame (s)	60	60	60
Standard deviation of gain fluctuation (ppm)	100	100	100
Dark current (electron s^{-1})	1.0	1.0	1.0
Readout noise (electron/read)	5.5	5.5	5.5

for earlier spectral types of stars, but the signal-to-noise ratio increases.

Once the residual (systematic) and random errors of this simulation system were evaluated, the spectrum data, including the derived errors, were compared with the theoretical transmission and emission spectra of a transiting Earth-like planet for each simulation case. The atmospheric composition of the transiting planet was similar to that of the Earth. There

are a number of absorption lines over 3–22 μm : CH₄ at 3.3 and 7.6 μm , O₃ at 4.75 and 9.6 μm , CO₂ at 4.3 and 15 μm , and H₂O around 6.3 and beyond 17 μm , respectively. The transmission and emission spectra of the four target planets were generated through the planetary spectrum generator (Villanueva et al. 2015). Figure 12 compares the theoretical transmission spectra of the Earth-like planet with the reconstructed one for the four simulation cases over wavelength ranges of 3–22 μm ; Figure 13 shows an enlarged view of the short band, 3–6 μm , in Figure 12. In addition, Figure 14 compares the emission spectra of the Earth-like planet with the reconstructed spectra for the four simulation cases. The important absorption features, including H₂O, CH₄, O₃, and CO₂, can be detected from the reconstructed transmission spectra of planets orbiting the M-type stars. Measurement of both oxidized species of O₃ and reduced species of CH₄ may confirm whether a nonequilibrium atmosphere indicates biological activity on a planet. In addition, the effective temperatures of the planets, as information concerning habitability, can also be measured through secondary eclipses. In contrast, the absorption features are embedded in the systematic and random components for the late-K-type star. Thus, this proposed calibration method contributes to the measurement of the habitability and biosignature of the nearby Earth-like planets orbiting late-type stars through both the transmission spectroscopy and secondary eclipse of the planets.

5. Discussion

5.1. Dependence of the Signal-to-noise Ratios of Background and Reference Pixels upon Calibration Accuracy

In Section 4, we used the background and reference data to calibrate the time-variation components. The calibration accuracy depends upon the signal-to-noise ratios of the background and reference pixels. Note that, while the signal-to-noise ratio of each background pixel changes with the radius of the field of view, as well as the brightness of the zodiacal

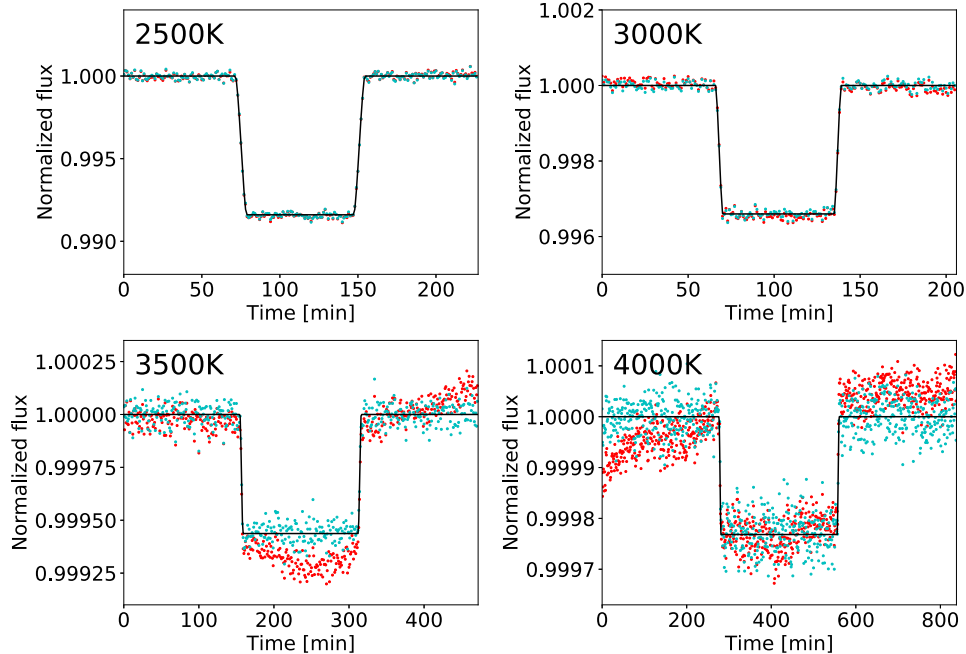


Figure 7. Input transit light curves (black line), original transit data without calibration (red points), and calibrated transit data (cyan points) at the observing wavelength of $10\text{ }\mu\text{m}$ for primary transits of transiting terrestrial planets orbiting four host stars with different effective temperatures of 2500, 3000, 3500, and 4000 K, corresponding to the four simulation cases.

light, each reference pixel depends upon the level of the dark current and readout noise. In this subsection, we discuss how the spectrophotometric accuracy changes for various signal-to-noise ratios of the background and reference pixels, respectively.

5.1.1. Signal-to-noise Ratio of the Background Pixels

While the proposed calibration method reduces the systematic noise to random noise for the late- and mid-M-type stars, slight offsets remain for the early-M- and late-K-type stars. This is because the second-order fluctuation represented in Equation (28) still remains after the calibration and contributes to the calibrated data as systematic noise. Here the second-order fluctuation is expected to be minimized when the calibrated data become closer to the ideal photon noise limit thanks to a high signal-to-noise ratio of the background pixel. In contrast, as the signal-to-noise ratio of the background pixel increases (i.e., the number of incident photons increases in the background pixel), the photon noise from the background light increases in the science pixel; the signal-to-noise ratio of the science pixel decreases.

We have examined how the level of the background light or the radius of the field stop affect the calibration accuracy. Figure 15 shows how the photometric accuracy for each spectral element depends upon the radius of the field of view. Note that the larger field of view is equal to an increase in the zodiacal light. For the case of the larger field of view, while the photometric accuracy for each spectral element can be improved over the shorter-wavelength range thanks to the higher signal-to-noise ratio of the background pixel, the photometric accuracy worsens in the longer-wavelength range, especially for the late- and mid-M-type stars, because of the larger photon noise in the science pixel.

5.1.2. Signal-to-noise Ratio of the Reference Pixels

The signal-to-noise ratio of the reference pixel depends upon the level of the dark current and the readout noise. The calibration accuracy is affected by the signal-to-noise ratios of the reference and background pixels. Although the dark current was fixed to $1.0\text{ }e^- \text{s}^{-1}$ in the previous simulation based on the performance of the MCT and Si:As detector systems, the dependency of the dark current level on the calibration method has been investigated.

Figure 16 shows the residual errors associated with the calibrated data for various levels of the dark current for the primary transit of each simulation case with various dark currents of 0.2 , 0.5 , 1.0 , and $5.0\text{ }e^- \text{s}^{-1}$. The higher dark current level improves the calibration technique, except over the longer-wavelength range of late- and mid-M-type stars. Thus, the dark current level is an important parameter for transit spectroscopy around early-type stars. Note that, because a higher dark current level requires a higher temperature of the detector system (e.g., Ennico et al. 2003), the higher dark current may have an impact on cryogenic space observatories such as the *Origins Space Telescope*.

5.2. Impact of Time Variation of Background Light and Dark Current upon the Calibration Method

So far, we have assumed that the zodiacal light and dark current are constant; however, actually, the signals have small time-variation components. Here we discuss how these time variations affect the proposed method.

5.2.1. Time Variation of Background Light

In previous sections, the background light was treated as a constant value; the background component, except for the zodiacal and galactic planes, is thought to be smooth on the

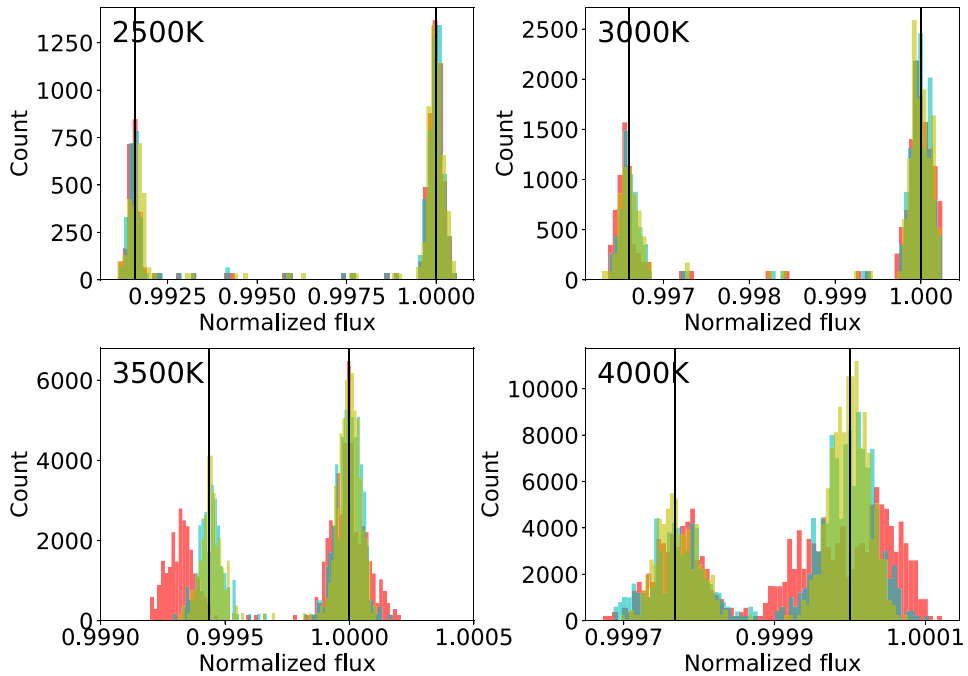


Figure 8. Histograms of original transit data without calibration (red bins), calibrated data (cyan bins), and ideal transit data with only photon noise (yellow bins) at the observing wavelength of $10\text{ }\mu\text{m}$ for the average transit data over 60 primary transits of the four simulation cases. The two vertical lines for each simulation case represent the two average values of the transit data in transit and out of transit, respectively.

timescale of a transit observation because the spatial distribution of zodiacal dust is mainly determined by the gravity field of the Sun and the solar system planets (Kondo et al. 2016). However, since the spatial variation of the zodiacal light at a high spatial scale ($\sim 1''$) is as yet unrevealed due to a lack of high angular resolution observations at mid-infrared wavelengths, there may be time variations of the zodiacal light over a timescale of a few hours due to its spatial brightness variation.

Here we considered the effect of the small time variation of the background pixels upon the proposed method and performed numerical simulations to evaluate how the effect degrades the calibration accuracy. Figure 17 shows the residual systematic errors associated with the calibrated data in the primary transit of each simulation case for various standard deviations of the zodiacal light time variation of 0, 100, 200, 300, and 1000 ppm. The time variation of a few hundred ppm can be ignored for the late- and mid-M-type stars. By contrast, for the early-M- and late-K-type stars, the residual systematic errors are larger in the longer-wavelength range because larger time variation occurs due to the brighter zodiacal light.

5.2.2. Time Variation of the Reference Pixels

Since the dark current in the ROIC depends on the detector temperature, we should consider the impact of time variation of the dark current upon the proposed method due to a small variation of the detector temperature. We evaluated the degradation of the calibration accuracy due to time variation of the dark current. Figure 18 shows the residual systematic errors associated with the calibrated data in the primary transit of each simulation case for standard deviations of the dark current time variation of 0, 100, 200, 300, and 1000 ppm. The effect of time variation of the dark current cannot be ignored

when the standard deviation is more than 100 ppm, because the signal-to-noise ratio of the averaged reference data over all reference pixels for each exposure is around 100 ppm. In addition, the time variation of the dark current largely affects the shorter band because the ratio of reference to science data that is used for reconstruction of the common time variation from the reference data is larger in the shorter-wavelength range (see Equation (25)).

There are two approaches for minimizing the impact of the dark current time variation on the method. The first is to stabilize the detector temperature, and the second is to measure the detector temperature and calibrate the dark current. Because the former approach is technically more difficult than the latter, the latter is discussed in this paper. Based on previous studies (i.e., Ennico et al. 2003; McMurtry et al. 2013), the relationship between the dark current and the detector temperature (i.e., the Arrhenius plot) can be expressed as

$$I_{\text{dark}} = C_1 10^{\frac{C_2}{T}}, \quad (33)$$

where C_1 and C_2 are constant values that depend upon the type of detectors and the detector temperature. When the dark current is $1\text{ }e^- \text{s}^{-1}$, the detector temperature should be measured down to 0.15 mK at 30 K for the MCT detector and 0.02 mK at 8 K for the Si:As detector to determine the dark current time variation with an accuracy of 100 ppm. Here, focusing on the fact that the proposed method does not require the absolute accuracy of the detector temperature but the relative one, commercially available cryogenic temperature sensors (i.e., Yeager & Courts 2001) can meet the above strict requirements on the relative temperature measurement mode (Courts et al. 1994). The resolvable temperature in the relative temperature measurement mode can be enhanced by a factor of

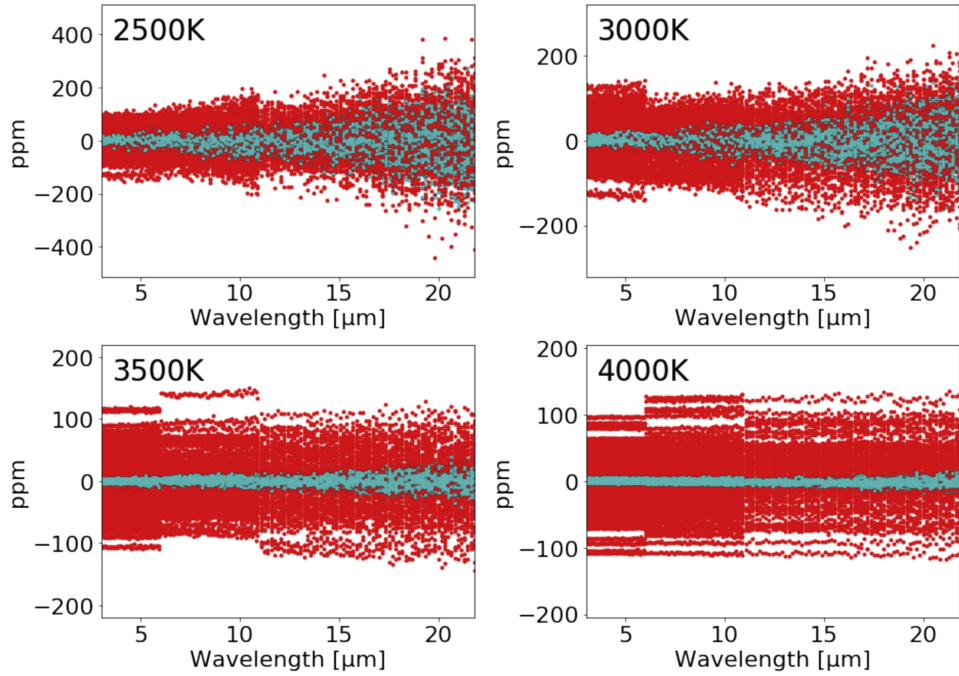


Figure 9. Residuals between the input model data and the raw (red) or calibrated (cyan) data over the observing wavelength range of 3–22 μm for the primary transits of the four simulation cases. The number of iterations for each wavelength was 100. Because the mean of the plots for each wavelength equals almost zero for the calibrated data, the systematic error associated with the raw data is reduced to the random component. The standard deviation of the plots for each wavelength is defined as the residual error. As the wavelength is longer, the residual error of the calibrated simulation system is larger because of the larger photon noise. The gaps seen in the early-M- and late-K-type stars in particular occur due to the limited number of simulations.

$\frac{V}{\Delta V}$ compared to that of the absolute mode, where V is the voltage required for a full measurement range in the absolute temperature measurement mode and ΔV is the variation of voltage during measurement. Thus, two cryogenic temperature sensors with absolute and relative temperature measurements may be sufficient to establish the proposed method.

5.3. Three Unconsidered Factors

There are four factors that are not considered for the numerical simulations discussed in the previous section. The first unconsidered factor is the estimation error of the offset components that is caused by adding residual carriers present in the last frame to those in the current frame. These residual carriers are generated by the electron capturing in the blocking layer of the semiconductor device and dielectric relaxation because of its long RC time constant (Rieke et al. 2015) and the persistence effect in the multiplexers of the ROIC (Beichman et al. 2014). The latent effect also leads to the estimation error of the offset voltage, thus affecting the calibration method. The second factor is the second-order effect of the metal-oxide semiconductor field effect transistors (MOSFETs) in the ROIC. The second-order effect mainly arises from the following four phenomena: channel-length modulation effect, substrate effect, short channel effect, and subthreshold region effect. The second-order effects also generate artifact time-variation components. The last systematic error is observed as a steep ramp in the beginning of the observations. The steep ramp arises from a gradual decrease in the recapture rate of photoelectrons in the semiconductor device. As introduced in

Section 2, because the recapture rate depends on the number of holes that capture the photoelectrons, the recapture rate decreases as the photoelectrons bury the holes. As the target object is brighter and the observing wavelength is closer to the peak of the spectrum, the recapture rate is thought to more rapidly decrease and further affect the measurement of the transit spectroscopy. Note that, although the decrease of the photometry curve over a timescale of 10 hr after the ramp may also affect phase-curve measurements, the impact of the fallback on transit spectroscopy is not discussed here because its amplitude is smaller than that of the ramp.

As discussed in Section 2, densified pupil spectroscopy that forms multiple spectra on the detector plane can mitigate various systematic errors. However, the systematic components potentially reduce the usefulness of the calibration method. The above three components are organized into two categories. One is the latent effect and second-order effect that contribute to the estimation error of the offset voltage. The other is a gradual increase in the effective gain due to electron trapping at the beginning of the transit observation. When the latent and second-order effects produce the offset voltages, ΔV_{back} and ΔV_{ref} , in the background and reference pixels, respectively, Equation (28) without the quadratic term changes to

$$\begin{aligned} v_{\text{sub,norm}}(\lambda, t) \\ \approx 1 + \frac{\delta f_s(\lambda, t)}{\langle f_s(\lambda) \rangle_i} + \sigma_{\text{sub,norm}}(\lambda) + v_{\text{offset}}(\lambda, t), \end{aligned} \quad (34)$$

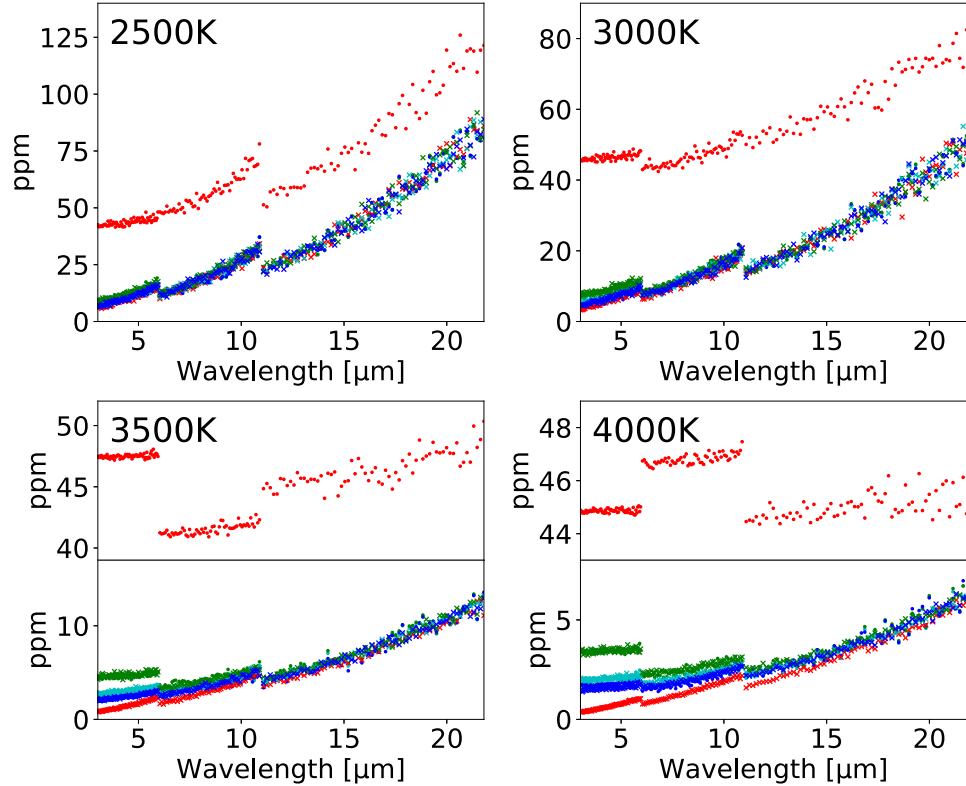


Figure 10. Comparison of the raw data with three types of calibrated data over the wavelength range of 3–22 μm for the primary transits in the four simulation cases. The red points represent the absolute values of the systematic errors attached to the raw data. The green, cyan, and blue points represent residual errors after calibration with three types of data: only background data, both reference and background data, and only reference data, respectively. The red, green, cyan, and blue crosses are the standard deviations of the random error before and after the calibration process with each signal, respectively. The residual error of the data reduced through the calibration is almost consistent with the random one for the four calibrated data because the systematic error associated with the raw data is reduced to the random component.

where v_{offset} is an offset component in the transit curve normalized by the source flux:

$$\begin{aligned} v_{\text{offset}}(\lambda, t) \\ \approx & \left(1 - \frac{\langle A_{\text{com}}(t) \rangle_t \{ f_z(\lambda) + 2 \langle I_{\text{dark},ij} \rangle_{\text{pix}} \}}{\langle A_{\text{com}}(t) \rangle_t \{ f_z(\lambda) + 2 \langle I_{\text{dark},ij} \rangle_{\text{pix}} \} + \Delta V_{\text{back}} + \Delta V_{\text{ref}}} \right) \\ & \times \left\{ 1 + \frac{f_z(\lambda) + \langle I_{\text{dark},ij} \rangle_{\text{pix}}}{\langle f_s(\lambda, t) \rangle_t} \right\} \frac{\delta A_{\text{com}}(t)}{\langle A_{\text{com}}(t) \rangle_t}. \end{aligned} \quad (35)$$

The estimation error of the offset voltage for the pixel-averaged background and reference pixels leaves the systematic component of $\frac{\delta A_{\text{com}}(t)}{\langle A_{\text{com}}(t) \rangle_t}$ in the calibrated transit data. As shown in Equation (35), when the gain variation, $\frac{\delta A_{\text{com}}(t)}{\langle A_{\text{com}}(t) \rangle_t}$, is small, this estimation error can be ignored. Figure 19 shows the residual systematic errors over the wavelength range of 3–22 μm for the various estimation errors of the offset voltage. The effect of the estimation error of the offset voltage on the proposed method can be ignored except for the short-wavelength ranges of the early-M- and late-K-type stars.

Last, we discuss the impact of the increase of the effective gain arising from the decrease in the recapture rate of photoelectrons on the transit spectroscopy. According to a previous study (Crossfield et al. 2012), the time variation of the signal due to the electron trapping can be formulated as a

function of time, $\beta(t)$,

$$\beta(t) = (1 - ae^{-\frac{t}{\tau_1}}) \times e^{-\frac{t}{\tau_2}}, \quad (36)$$

where τ_1 and τ_2 are timescales of the ramp and fallback with $\tau_2 > \tau_1$, respectively, and a is a free parameter depending on the signal value. Here, focusing on the fact that the number of photons falling on each pixel from a target object is much reduced owing to the multiple spectra formed on the detector plane, the timescales of the ramp and fallback are much longer than that of the general-purpose spectrograph:

$$\beta(t) \approx 1 - ae^{-\frac{t}{\tau_1}}. \quad (37)$$

Here τ_1 for the densified pupil spectrograph is recalculated using τ_1 and a derived for the transit observations of the HD 209458 system conducted with the multiband imaging photometer for *Spitzer* (Crossfield et al. 2012; Table 3). Note that a is fixed and τ_1 is assumed to be inversely proportional to the number of photons falling on a pixel. When $\beta_{\text{sci}}(t)$ in the science pixel has a fluctuation component with an amplitude of $\delta\beta_{\text{sci}}(\lambda, t)$ over one transit observation, Equation (28) without the quadratic term is rewritten as

$$v_{\text{sub,norm}}(\lambda, t) \approx 1 + \frac{\delta f_s(\lambda, t)}{\langle f_s(\lambda) \rangle_t} + \sigma_{\text{sub,norm}}(\lambda) + v_{\text{beta}}(\lambda, t), \quad (38)$$

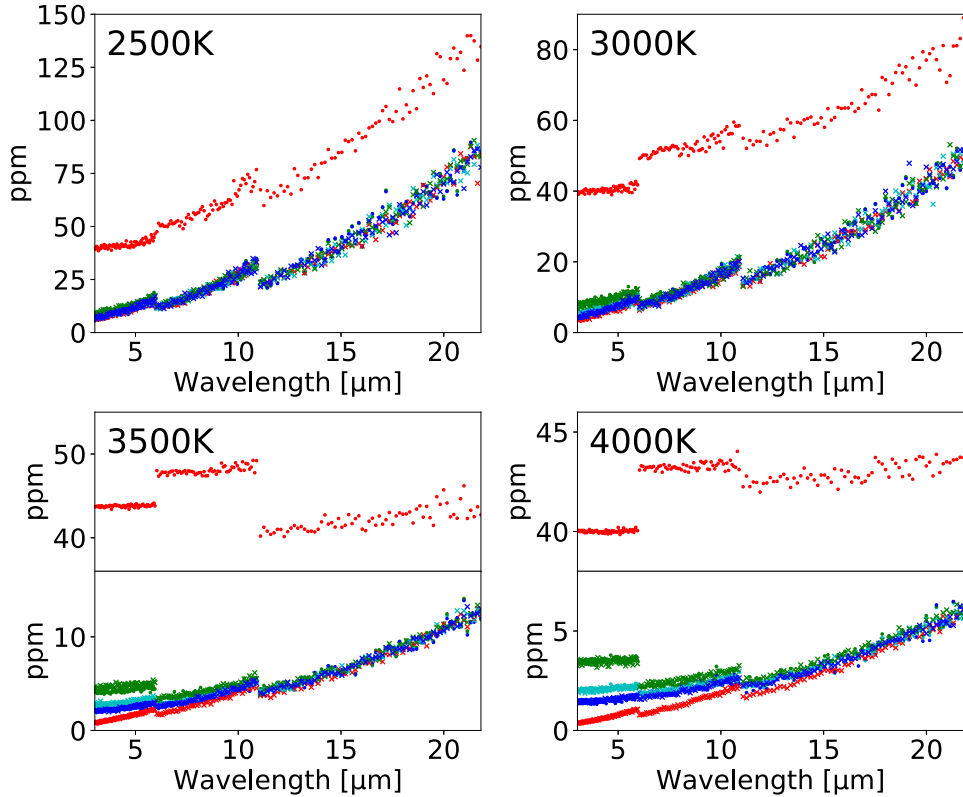


Figure 11. Comparison of the raw data with three types of calibrated data over the wavelength range of 3–22 μm for the secondary eclipses in the four simulation cases. The symbols are the same as in Figure 10. Because the residual errors for the secondary eclipses are the same as those for the primary transits, the photometric accuracy after the calibration does not depend on the input signal.

where $v_{\beta\text{eta}}(\lambda, t)$ is the residual error caused by the fluctuation of $\beta_{\text{sci}}(t)$:

$$v_{\beta\text{eta}}(\lambda, t) \approx \left\{ 1 + \frac{f_z(\lambda) + \langle I_{\text{dark},ij} \rangle_{\text{pix}}}{\langle f_s(\lambda) \rangle_t} \right\} \frac{\delta\beta_{\text{sci}}(\lambda, t)}{\langle \beta_{\text{sci}}(\lambda) \rangle_t}. \quad (39)$$

The residual error cannot be reduced through the calibration method and directly affects the transit measurements. Table 4 shows the impacts of the decrease in the recapture rate on the relative spectrophotometric accuracies for the whole observing wavelength range of 3–22 μm , the methane feature between 3.2 and 3.5 μm , the ozone feature between 9 and 10 μm , and the carbon dioxide feature between 13 and 17 μm . The spectrophotometric accuracies for observations of the late- and mid-M-type stars fully agree with the measurements of dayside emission and absorption features. This occurs because the timescales of the ramp for the late- and mid-M-type stars are much longer than those for general-purpose spectrographs, owing to the relatively small number of photons falling on each pixel. However, it is difficult to perform the transmission spectroscopy and secondary eclipse of terrestrial planets orbiting early-M- and late-K-type stars, even for the densified pupil spectrograph without any additional treatment.

6. Summary

We proposed a new method for mitigation and calibration of time-variation components present in the detector system,

developing the densified pupil spectrograph that forms multiple spectra of divided primary mirrors on the detector plane to mitigate the impact of the WFE in the optical system on the transit spectroscopy. In addition, a number of science pixels largely reduce the number of photons falling on each pixel and mitigate the ramp at the beginning of the transit observation, the fallback after the ramp, and the latent effect. The pixel-to-pixel time variations can also be smoothed out, and the common time-variation components extracted, through an average of a number of science pixels. Here, focusing on the fact that the detector plane is optically conjugated to the primary mirror, a number of black-off pixels, called reference pixels, are formed by putting a mask on the pupil plane. Furthermore, placing an additional grating with a different angle from the one used for the science light on the focal plane would result in part of the detector format being illuminated by only the background light (i.e., background pixels). Since the common time-variation components also affect the signals of the background and reference pixels, the components can be reconstructed from these pixels. The background light included in the science pixels can be removed through subtraction of background pixels from science ones. Finally, the pixel-averaged science pixels are composed of the transit signal and random components. Note that the reduced random components after the calibration processes are enhanced by the shot noise of the background and reference pixels because the systematic components are reconstructed using the background and reference pixels.

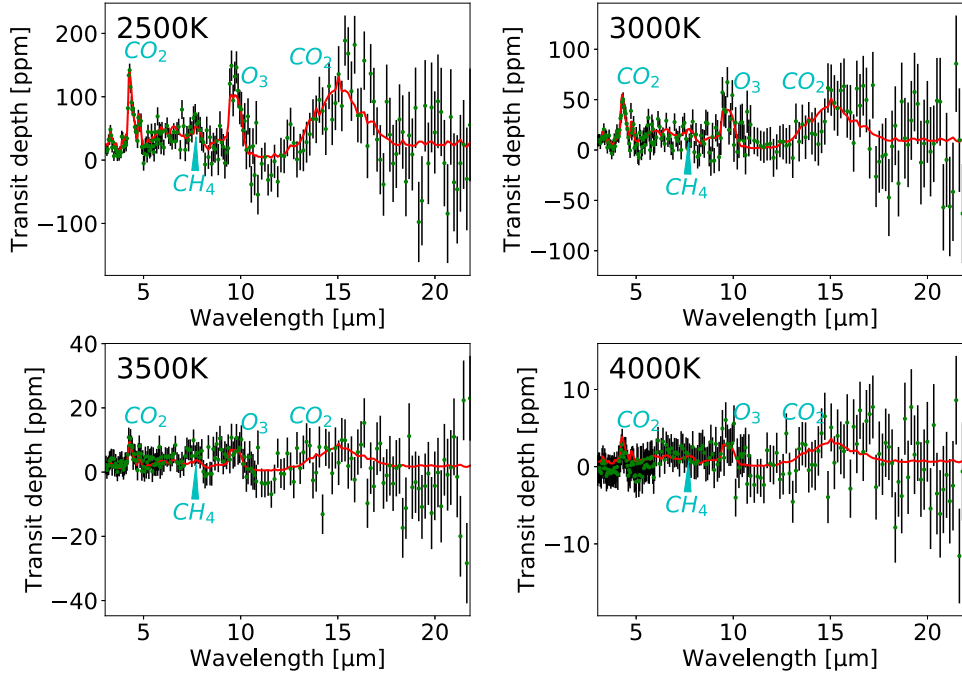


Figure 12. Theoretical transmission spectra (red solid line) and reconstructed spectra (green points) of Earth-like planets orbiting four host stars with different effective temperatures of 2500, 3000, 3500, and 4000 K in the wavelength range of 3–22 μm . The spectra are reconstructed through 60 transit observations with the densified pupil spectrograph mounted on a 9.3 m diameter telescope. The black vertical line attached to each green point represents the standard deviation of the random component associated with the calibrated data. The theoretical transmission spectra of the Earth-like planets were generated through the planetary spectrum generator (Villanueva et al. 2015).

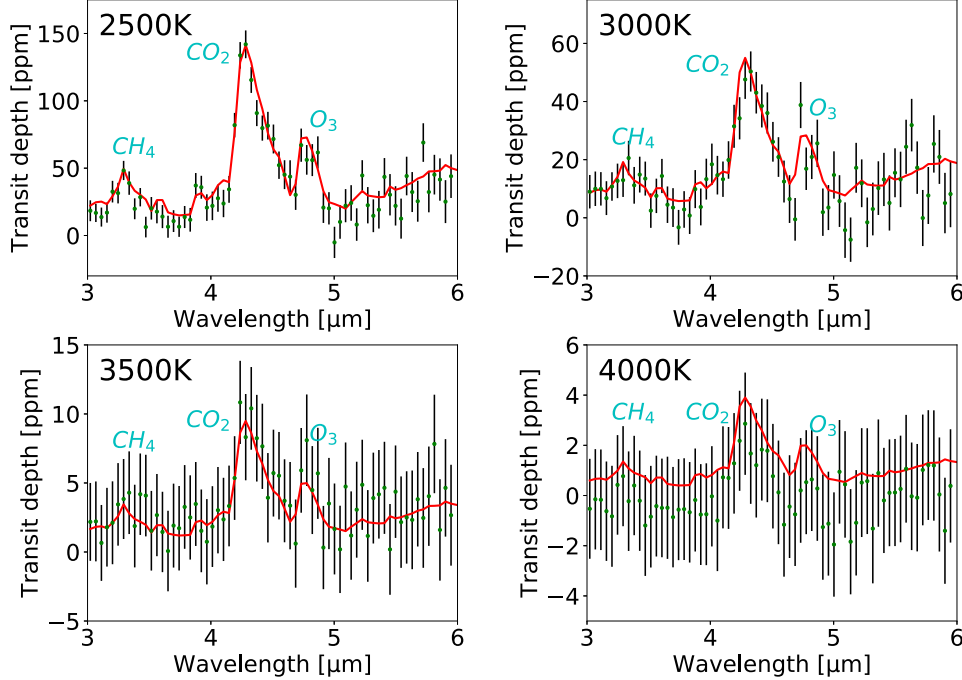


Figure 13. Enlarged views of the short bands, 3–6 μm , for the four simulation cases in Figure 12. The symbols are the same as in Figure 12.

We confirmed that the proposed method for calibration of the common systematic components over the entire detector plane is validated for the mid-infrared detector systems through

mathematical analysis. We also performed numerical simulations to investigate whether the method effectively works under realistic assumptions. Sixty transit observations for

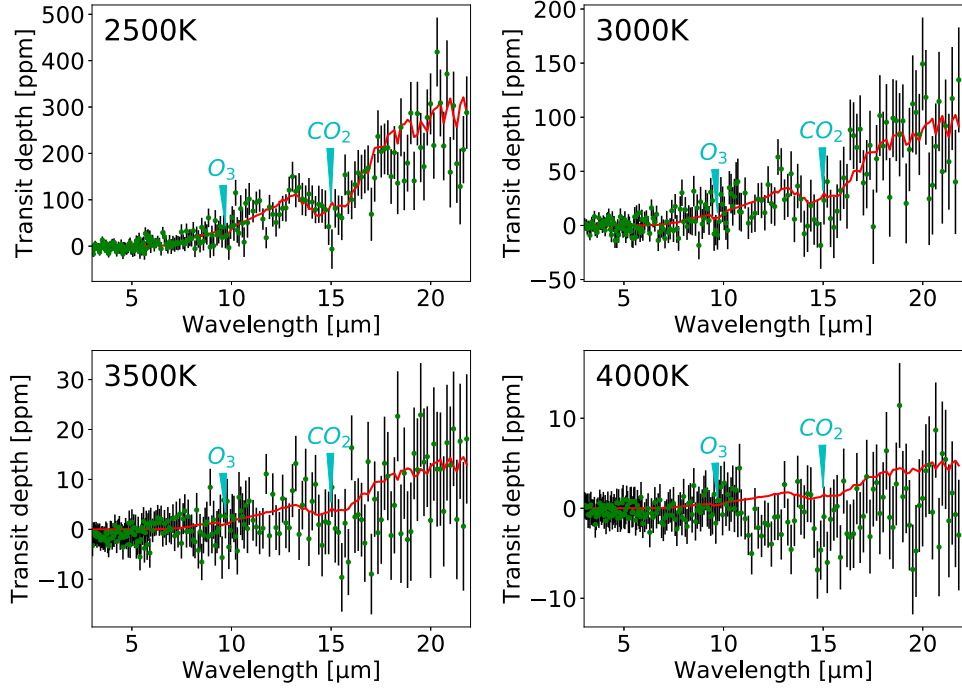


Figure 14. Theoretical emission spectra (red solid line) and reconstructed spectra (green points) of Earth-like planets orbiting four host stars with different effective temperatures of 2500, 3000, 3500, and 4000 K in the wavelength range of 3–22 μm . The symbols are the same as in Figure 12.

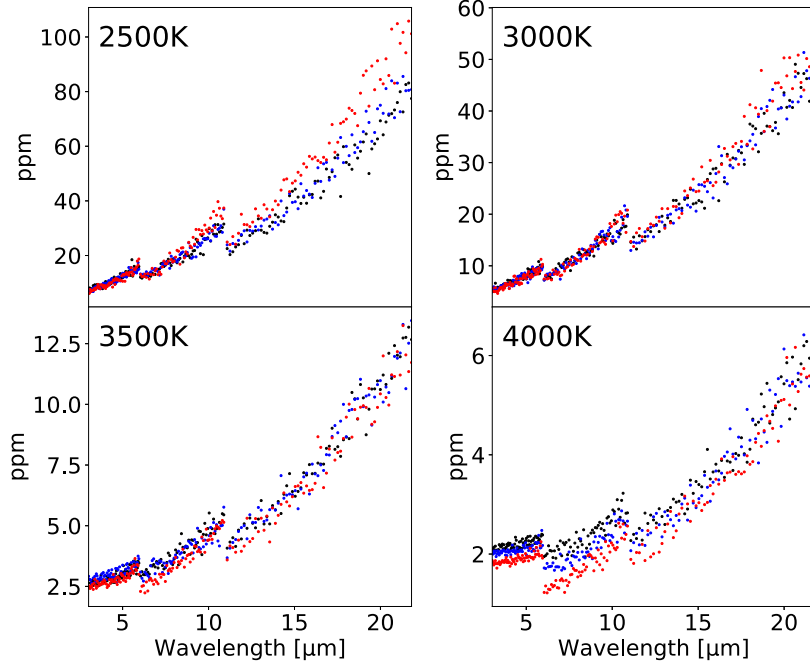


Figure 15. Residual systematic noise of the calibrated data with both the background and reference pixels over the wavelength range of 3–22 μm for the primary transits of the four simulation cases. Fields of view are 1.0 (black points), 2.0 (blue points), and 4.0'' (red points) in radius. Because the residual errors associated with the calibrated data include the shot noise of the zodiacal light, the residual error is further reduced as the radius of the field of view increases, except over the longer-wavelength range for late- and mid-M-type stars.

transmission spectroscopy and the secondary eclipse of terrestrial planets orbiting four host stars with different effective temperatures of 2500, 3000, 3500, and 4000 K at

10 pc were performed with the densified pupil spectrograph mounted on the *Origins Space Telescope* having a 9.3 m primary mirror. We found that the method successfully reduced

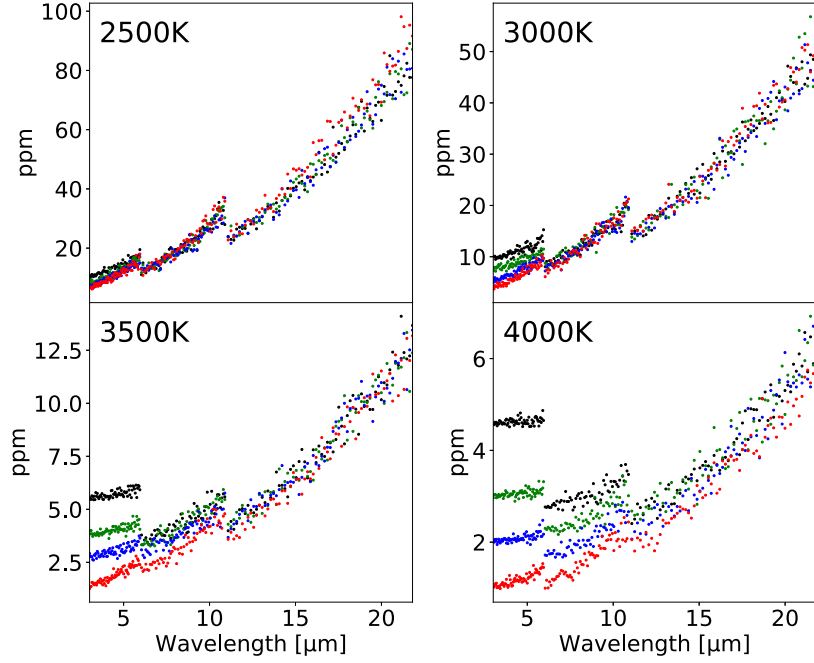


Figure 16. Residual systematic noises of the calibrated data over the wavelength range of 3–22 μm in the primary transits of each simulation case for the various dark current levels of 0.2 (black points), 0.5 (green points), 1.0 (blue points), and 5.0 (red points) $e^- \text{s}^{-1}$. Because the residual errors associated with the calibrated data include the shot noise of the dark current, the residual error is further reduced as the dark current increases.

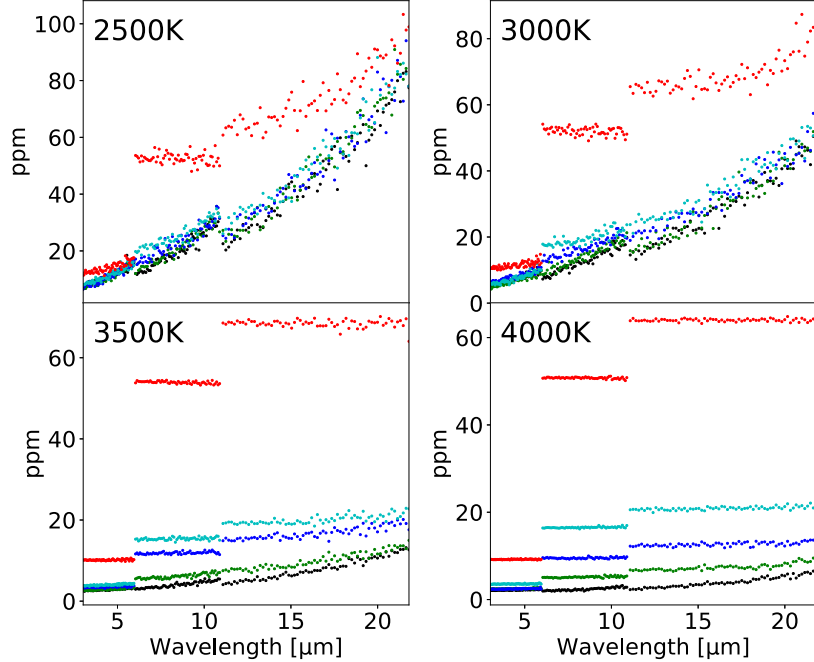


Figure 17. Residual systematic noise of the calibrated data with both background and reference pixels over the wavelength range of 3–22 μm for the primary transits of the four simulation cases with various standard deviations of the time fluctuation of zodiacal light. The black, green, blue, cyan, and red points show the residual systematic errors for the standard deviations of 0, 100, 200, 300, and 1000 ppm, respectively.

the systematic components to the random ones and nearly reached the photon noise-limited performance for the temperatures of 2500, 3000, and 3500 K. The proposed method contributes to the measurement of the biosignature and

habitability of terrestrial planets orbiting M-type stars. However, the systematic components for the late-K-type stars remain, because the second-order fluctuation affects the calibration method. In addition, the random components are

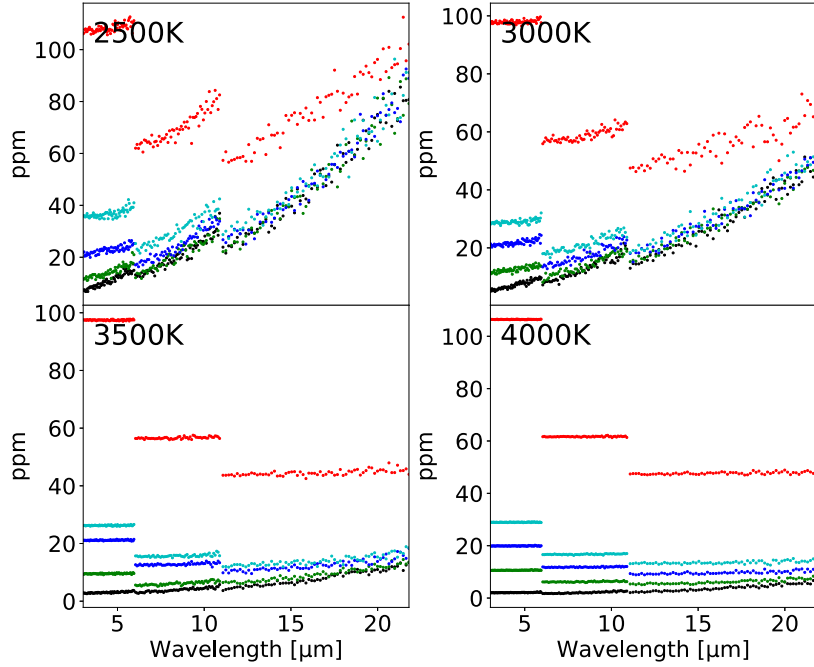


Figure 18. Residual systematic noises of the calibrated data over the wavelength range 3–22 μm in the primary transits of each simulation case for various standard deviations of the time fluctuation of the dark current. The black, green, blue, cyan, and red points show the residual systematic errors for standard deviations of 0, 100, 200, 300, and 1000 ppm, respectively.

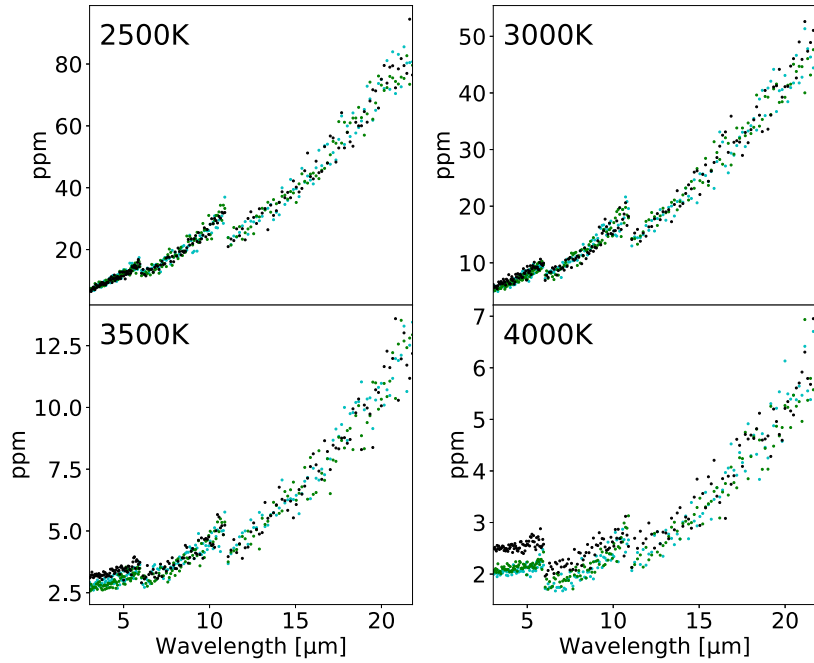


Figure 19. Residual systematic noise of the calibrated data over the wavelength range of 3–22 μm in the primary transits of each simulation case for estimation errors of the offset voltage of 0% (cyan points), 10% (green points), and 50% (black points).

slightly enhanced through the calibration process compared to the shot noise associated with the raw data and limit the final spectrophotometric accuracy. Here we succeeded in mitigation of the residual offset error through enhancement of the signal-to-noise ratios of the background and reference pixels.

Finally, we investigated the impacts of the signal-to-noise ratios of the background and reference pixels. Higher ratios improve the calibration technique, except at the longer wavelengths of late- and mid-M-type stars. We also studied the impact of time variations of the background light and dark

Table 3
Values of a and τ_1 Used for Equation (37)

Items	Case 1 ^a	Case 2 ^a	Case 3 ^a	Case 4 ^a	HD 209458 ^b
a^c	0.02	0.02	0.02	0.02	0.02
τ_1^d at $3 \mu\text{m}$ (hr)	135	37	4	1	...
τ_1^d at $10 \mu\text{m}$ (hr)	1185	379	51	18	...
τ_1^d at $15 \mu\text{m}$ (hr)	1854	605	83	29	...
τ_1^d at $22 \mu\text{m}$ (hr)	5307	1751	244	86	...
τ_1^d at $24 \mu\text{m}$ (hr)	10

Notes.^a Cases 1–4 correspond to the four simulation cases introduced in Section 4.^b HD 209458 was observed in the MIPS $24 \mu\text{m}$ band (Crossfield et al. 2012).^c Here a was directly estimated from the result of Crossfield et al. (2012).^d Here τ_1 was derived under an assumption that the timescale is determined only by the number of photons falling on each pixel.

Table 4
Relative Spectrophotometric Errors Arising from Electron Trapping for the Four Simulation Cases

Wavelength Band	Case 1 (ppm)	Case 2 (ppm)	Case 3 (ppm)	Case 4 (ppm)
Whole observing wavelength range of $3\text{--}22 \mu\text{m}$	0.9	9	1465	2798
Methane band between 3.2 and $3.5 \mu\text{m}$	0.2	2	315	210
Ozone band between 9 and $10 \mu\text{m}$	0.009	0.06	16	295
Carbon dioxide band between 13 and $17 \mu\text{m}$	0.009	0.07	19	276

current on the proposed method and found that the fluctuations of zodiacal light and dark current should be reduced down to 100 ppm. In terms of reducing the impact of the drift of the dark current during transit observation, we can measure the fluctuation of the detector temperature and calibrate the time variation of the dark current instead of stabilizing the detector temperature. Note that the small fluctuation of the detector temperature can be measured using the relative temperature measurement mode of commercially available cryogenic sensors. Next, we investigated the ramp over the transit light curve due to the trapping effect and the estimation error of the offset voltage on the transit spectroscopy. Assuming that the timescale of the ramp is proportional to the number of photons falling on each pixel, the timescale for the densified pupil spectrograph is expected to be much longer than those of general-purpose spectrographs, because the densified pupil spectrograph forms multiple spectra on the detector plane. However, because bright stars with an effective temperature

higher than 3500 K at 10 pc generate a large number of photons falling on each pixel, even for the densified pupil spectrograph, the relative spectrophotometric accuracies between wavelengths are limited by the ramp. The estimation error of the offset voltage also produces systematic components that influence the transit spectroscopy. By contrast, the effects of the estimation error of the offset voltage and the latent image upon the proposed method can be ignored unless the time variation of the gain is not small.

We are building a prototype of the densified pupil spectrograph optimized for the mid-infrared wavelength range and will demonstrate the proposed method, imitating an observing environment of the *Origins Space Observatory*.

Appendix Parameters and Assumptions

The parameters and their assumptions used for formulation and numerical simulations are compiled in Table 5.

Table 5
Parameters and Their Assumptions for Formulation and Numerical Simulations

Parameters	Explanations	Assumptions
η_{ij}	Quantum efficiency of (i, j) pixel	Fixed constant in each pixel
α_{ij}	Effective pixel gain of (i, j) pixel	Fixed constant in each pixel
β_{ij}	Effective gain of (i, j) pixel related to electron trapping	Fixed constant in each pixel in Sections 2–4 and variable in Section 5
$f_{s,ij}$	Number of photons from an object source falling on (i, j) pixel	Common variable over the science pixels due to shot noise and planetary transit
$f_{z,ij}$	Number of photons from zodiacal light falling on (i, j) pixel	Variable in each pixel due to shot noise
t_{exp}	Exposure time	Fixed constant of 60 s
C_{ij}	Capacitor capacitance in (i, j) pixel unit	Fixed constant in each pixel
$I_{\text{dark},ij}$	Dark current of (i, j) pixel	Variable in each pixel attaching shot noise
I_j	Common current of j th column	Variable in each column
I_k	Common current in k th gate	Variable in each gate
A_{ij}	Transfer function of source follower in (i, j) pixel unit	Variable in each pixel
A_k	Transfer function of k th source follower	Variable in each gate
$V_{\text{det},ij}$	Detector bias voltage	Fixed constant in each pixel
V_{dduc}	Drain voltage at source follower in each pixel unit	Fixed constant in each pixel
V_{ddout}	Drain voltage at source follower in readout gate	Fixed constant in each gate
$V_{\text{res},ij}$	Reset voltage in (i, j) pixel unit	Variable in each pixel including shot noise present in (i, j) pixel
$v_{\text{int},ij}$	Integrated voltage of (i, j) pixel at source follower of (i, j) pixel unit	Variable in each pixel including shot noise present in (i, j) pixel
$v_{\text{out},ijk}$	Output voltage of (i, j) pixel at source follower at k th readout gate	Variable in each pixel including shot noise present in (i, j) pixel
$v_{\text{sci},ijk}$	Output voltage of (i, j) science pixel with k th readout gate	Variable in each pixel attaching
$v_{\text{back},ijk}$	Output voltage of (i, j) background pixel with k th readout gate	Variable in each pixel attaching shot noise of zodiacal light
$v_{\text{ref},ijk}$	Output voltage of (i, j) reference pixel with k th readout gate	Variable in each pixel attaching shot noise of dark current
n_{sci}	Number of science pixels for spectrally resolved band	Fixed constant of 120,000
n_{back}	Number of background pixels for spectrally resolved band	Fixed constant of 120,000
n_{ref}	Number of reference pixels	Fixed constant of 760,000

ORCID iDs

Shohei Goda  <https://orcid.org/0000-0002-6228-1667>

References

- Agol, E., Cowan, N. B., Knutson, H. A., et al. 2010, ApJ, 721, 1861
 Angel, J. R. P., & Woolf, N. J. 1997, ApJ, 475, 373
 Ballerini, P., Micela, G., Lanza, A. F., & Pagano, I. 2012, A&A, 539, A140
 Barron, N., Borysow, M., Beyerlein, K., et al. 2007, PASP, 119, 466
 Barstow, J. K., & Irwin, P. G. J. 2016, MNRAS, 461, L92
 Beichman, C., Benneke, B., Knutson, H., et al. 2014, PASP, 126, 1134
 Beichman, C. A., & Greene, T. P. 2018, arXiv:1803.03730
 Boyajian, T. S., von Braun, K., van Belle, G., et al. 2012, ApJ, 757, 112
 Boyajian, T. S., von Braun, K., van Belle, G., et al. 2017, ApJ, 845, 178
 Bracewell, R. N. 1978, Natur, 274, 780
 Carey, S., Ingalls, J., Grillmair, C., & Krick, J. 2014, in ASP Conf. Ser. 485, Astronomical Data Analysis Software and Systems XXIII., ed. N. Manset & P. Forshay (San Francisco, CA: ASP), 407
 Cash, W. 2006, Natur, 442, 51
 Charbonneau, D., Brown, T. M., Noyes, R. W., & Gilliland, R. L. 2002, ApJ, 568, 377
 Charbonneau, D., Knutson, H. A., Barman, T., et al. 2008, ApJ, 686, 1341
 Courts, S. S., Holmes, D. S., & Swinehart, P. R. 1994, Radiation Resistant Cryogenic Temperature Sensor for the 4 K to 80 K Range, Final Rep. Dept. Energy, Contract DE-FG02-90ER81074 by Lake Shore Cryotronics Inc.
 Crossfield, I. J. M., Knutson, H., Fortney, J., et al. 2012, ApJ, 752, 81
 Deming, D., Seager, S., Richardson, L. J., & Harrington, J. 2005, Natur, 434, 740
 Deming, D., Seager, S., Winn, J., et al. 2009, PASP, 121, 952
 Ennico, K. A., McKelvey, M. E., McCreight, C. R., et al. 2003, Proc. SPIE, 4850, 890
 Fortney, J., Kataria, T., Stevenson, K., et al. 2018, arXiv:1803.07730
 Gillon, M., Triaud, A. H. M. J., Demory, B.-O., et al. 2017, Natur, 542, 456
 Greene, T. P., Line, M. R., Montero, C., et al. 2016, ApJ, 817, 17
 Ingalls, J. G., Krick, J. E., Carey, S. J., et al. 2012, Proc. SPIE, 8442, 84421Y
 Itoh, S., Matsuo, T., Goda, S., Shibai, H., & Sumi, T. 2017, AJ, 154, 97
 Johnson, J. F. 1999, ITED, 46, 96
 Johnson, J. F., & Lomheim, T. S. 2009, ITED, 56, 2506
 Kaltenegger, L. 2017, ARA&A, 55, 433
 Kaltenegger, L., & Traub, W. A. 2009, ApJ, 698, 519
 Kasting, J. F., Kopparapu, R., Ramirez, R. M., & Harman, C. E. 2014, PNAS, 111, 12641
 Kataria, T., Sing, D. K., Lewis, N. K., et al. 2016, ApJ, 821, 9
 Kelsall, T., Weiland, J. L., Franz, B. A., et al. 1998, ApJ, 508, 44
 Knutson, H. A., Charbonneau, D., Allen, L. E., et al. 2007, Natur, 447, 183
 Knutson, H. A., Charbonneau, D., Cowan, N. B., et al. 2009, ApJ, 703, 769
 Knutson, H. A., Madhusudhan, N., Cowan, N. B., et al. 2011, ApJ, 735, 27

- Kondo, T., Ishihara, D., Kaneda, H., et al. 2016, AJ, 151, 71
- Kump, L. R., & Barley, M. E. 2007, Natur, 448, 1033
- Lovelock, J. E. 1965, Natur, 207, 568
- Lyons, T. W., Reinhard, C. T., & Planavsky, N. J. 2014, Natur, 506, 307
- Madhusudhan, N., & Seager, S. 2009, ApJ, 707, 24
- Mann, A. W., Feiden, G. A., Gaidos, E., Boyajian, T., & von Braun, K. 2015, ApJ, 804, 64
- Matsuo, T., Greene, T., Roellig, T. L., et al. 2018, Proc. SPIE, 10698, 1069844
- Matsuo, T., Itoh, S., Shibai, H., Sumi, T., & Yamamoto, T. 2016, ApJ, 823, 139
- Matsuo, T., Traub, W. A., Hattori, M., & Tamura, M. 2011, ApJ, 729, 50
- McMurtry, C., Lee, D., Beletic, J., et al. 2013, Proc. SPIE, 1306, 6978
- Morello, G., Waldmann, I. P., & Tinetti, G. 2016, ApJ, 820, 86
- Perryman, M. 2011, *The Exoplanet Handbook*, Vol. 1 (1st ed.; New York: Cambridge Univ. Press)
- Rauscher, B. J. 2015, PASP, 127, 1144
- Rauscher, B. J., Arendt, R. G., Fixsen, D. J., et al. 2017, PASP, 129, 105003
- Rauscher, B. J., Boehm, N., Cagiano, S., et al. 2014, PASP, 126, 739
- Ressler, M. E., Sukhatme, K. G., Franklin, B. R., et al. 2015, PASP, 127, 675
- Rieke, G. H. 2007, ARA&A, 45, 77
- Rieke, G. H., Ressler, M. E., Morrison, J. E., et al. 2015, PASP, 127, 665
- Roberto, M. 2014, Tech. Rep., JWST-STScI-003852, SM-12
- Rugheimer, S., & Kaltenegger, L. 2018, ApJ, 854, 19
- Sagan, C., Thompson, W. R., Carlson, R., Gurnett, D., & Hord, C. 1993, Natur, 365, 715
- Seager, S., & Deming, D. 2009, ApJ, 703, 1884
- Stevenson, K. B., Désert, J.-M., Line, M. R., et al. 2014, Sci, 346, 838
- Swain, M. R., Vasisht, G., & Tinetti, G. 2008, Natur, 452, 329
- Tinetti, G., Vidal-Madjar, A., Liang, M.-C., et al. 2007, Natur, 448, 169
- Trauger, J. T., & Traub, W. A. 2007, Natur, 446, 771
- Van Grootel, V., Fernandes, C. S., Gillon, M., et al. 2018, ApJ, 853, 30
- Villanueva, G. L., Mumma, M. J., Novak, R. E., et al. 2015, Sci, 348, 218
- Vincent, J. D., Hodges, S. E., Vampola, J., Stegall, M., & Pierce, G. 2016, *Fundamentals of Infrared and Visible Detector Operation and Testing*, Vol. 2 (2nd ed.; Hoboken, New Jersey: Wiley)
- Waldmann, I. P., Tinetti, G., Deroo, P., et al. 2013, ApJ, 766, 7
- Yeager, C. J., & Courts, S. S. 2001, IEEE Sensors, 1, 352
- Young, E. T., Rieke, G. H., Cadien, J., et al. 2003, Proc. SPIE, 4850, 98
- Zellem, R. T., Lewis, N. K., Knutson, H. A., et al. 2014, ApJ, 790, 53